

This is an Open Access document downloaded from ORCA, Cardiff University's institutional repository: <https://orca.cardiff.ac.uk/id/eprint/164414/>

This is the author's version of a work that was submitted to / accepted for publication.

Citation for final published version:

Maguire, E. S. F., Barker, T., Rauter, M., Johnson, C. G. and Gray, J. M. N. T. 2024. Particle-size segregation patterns in a partially filled triangular rotating drum. *Journal of Fluid Mechanics* 979 , A40.
10.1017/jfm.2023.1022

Publishers page: <https://doi.org/10.1017/jfm.2023.1022>

Please note:

Changes made as a result of publishing processes such as copy-editing, formatting and page numbers may not be reflected in this version. For the definitive version of this publication, please refer to the published source. You are advised to consult the publisher's version if you wish to cite this paper.

This version is being made available in accordance with publisher policies. See <http://orca.cf.ac.uk/policies.html> for usage policies. Copyright and moral rights for publications made available in ORCA are retained by the copyright holders.



Banner appropriate to article type will appear here in typeset article

Particle-size segregation patterns in a partially filled triangular rotating drum

E.S.F. Maguire¹, T. Barker^{1,2}, M. Rauter³, C.G. Johnson¹ & J.M.N.T. Gray¹

¹Department of Mathematics and Manchester Centre for Nonlinear Dynamics, University of Manchester, Oxford Road, Manchester, M13 9PL, UK

²School of Mathematics, University of Cardiff, Cardiff, CF10 3AT, UK

³Department of Water Management, Office of the Tyrolean Regional Government, Innsbruck, Austria.

(Received xx; revised xx; accepted xx)

In this paper a fully coupled particle-size segregation model for granular flows (Barker, Rauter, Maguire, Johnson and Gray, *J. Fluid Mech.*, vol. 909, 2021, A22) is used to simulate the development of the patterns in a triangular rotating drum. The results are compared to the experimental patterns with bidisperse and tridisperse granular mixtures, and with varying compositions and fill heights. In all cases the agreement between the simulations and experiments is remarkably good. The experimental patterns are generated in a narrow gap between transparent front and back sidewalls. These prevent three-dimensional motion, but also impose friction on the flow, making it thinner and faster than it would otherwise be. This promotes segregation, as it simultaneously increases the shear rate and reduces the local pressure. To obtain the correct flow dynamics and segregation, width-averaged sidewall friction is incorporated into the two-dimensional simulations, which are performed in OpenFOAM[®]. The free-surface avalanche forms a boundary layer within which all the segregation occurs. Material in the lower reach of the avalanche is continuously deposited into an underlying solid body of grains, which rotates with the drum, and is eventually re-entrained into the avalanche along its upper reach. The changing geometry of the granular region (as the drum rotates) implies that the avalanche is constantly adjusting its length, position and depth. This generates a complex quasi-periodic flow, which when combined with particle-size segregation generates amazing patterns in the solid rotating granular body after only two drum rotations.

1. Introduction

Granular materials are abundant in the natural world, in industrial processes and in our everyday lives. Indeed, after fluids, granular materials are the most common material used by mankind in a wide range of processes in the bulk chemical, civil, pharmaceutical, mining, agricultural and food industries (Morrow 1984; Bates 1997; Shinbrot & Muzzio 2000; Richard *et al.* 2005). Despite their widespread use, our ability to model their behaviour using continuum theories lags far behind that of Computational Fluid Dynamics (CFD) for liquids. This is because the rheology of granular flows is more complex, and not yet fully understood (GDR MiDi 2004; Jop, Forterre & Pouliquen 2006), with aggregates of grains simultaneously behaving as a solid, a liquid or a gas in disparate spatially and temporally

evolving regions. Physicists and engineers have therefore relied heavily on Discrete Element Model/Discrete Particle Model (DEM/DPM) numerical simulations to understand particle flow behaviour and optimize the design of industrial systems (Cundall & Strack 1979; Silbert *et al.* 2001; Cleary & Sawley 2002; GDR MiDi 2004; da Cruz *et al.* 2005; Zhu *et al.* 2008; Ketterhagen *et al.* 2009; Chialvo *et al.* 2012; Weinhart *et al.* 2013; Vo *et al.* 2020). However, as the number of particles increases DEM/DPM simulations rapidly become prohibitively computationally expensive, which restricts their use to small systems, with usually less than a few million particles. There is therefore a pressing need to develop reliable and efficient continuum methods, that do not need to resolve each individual particle and particle collision.

As a prototypical example of a non-trivial granular flow, this paper focusses on the mixing and segregation of particles in a partially filled thin triangular rotating drum (Mounty 2007). Similar, flows in elliptical and square drums were first investigated by Hill *et al.* (1999) and Ottino & Khakhar (2000), who showed experimentally that the combination of flow and segregation produced beautiful quasi-periodic patterns. An example of the pattern formed in a triangular drum, 70% filled with a mixture of large green, medium white and small red glass beads, is shown in figure 1. The full time-dependent evolution can be seen in movie 1 (see supplementary material available online). Two arms of small and medium particles rapidly form, which radiate out from the central core towards the drum corners, forming a striking pattern. Experiments have also been performed in square, pentagonal and hexagonal drums (not shown) that also produce a series of arms, but with increasingly reduced amplitude. This paper therefore focusses exclusively on the triangular drum.

As the drum rotates, most of the grains are in solid body rotation, but a thin avalanche forms above a critical free surface angle and transports grains rapidly downslope. Grains in the avalanche are progressively deposited along its lower reach, and are slowly rotated (with the drum) back up to where they re-enter the avalanche along its upper reach. The flow is akin to that formed in the rolling regime of a circular rotating drum, where a steady-state avalanche can form (Henein *et al.* 1983; Rajchenbach 1990; Metcalfe *et al.* 1995; Gray & Hutter 1997; Gray 2001). However, unlike a circular drum, the geometrical shape occupied by the grains constantly changes as the triangular drum rotates, which precludes the formation of a steady state. As a result, the free-surface position as well as the maximum avalanche depth and length are functions of time. Hill *et al.* (1999) and Ottino & Khakhar (2000) showed that for mono-disperse particles rotating in elliptical and square drums, the resulting flow field leads to chaotic advection of tracer particles. A similar result holds for triangular drums (Mounty 2007). Moreover, if the drum is more than half full, then a central core of grains can form that are never entrained into the avalanche and essentially just rotate with the drum (although there is some very slow creep, Socie *et al.* 2005). This corresponds to the central green region in figure 1.

Particle-size segregation adds an important ordering mechanism on top of these deceptively simple chaotic flows. Particles in the slightly dilated rapidly-shearing thin surface avalanche, are able to segregate by size, with the largest grains being pushed towards the surface by force imbalances and the small grains percolating down to the base under the action of gravity (Gray & Ancy 2011; Gray 2018; Trewela, Ancy & Gray 2021). This leads to the development of an inversely-graded particle-size distribution, with the largest grains concentrated at the surface and the smallest ones at the base. In the lower reach of the avalanche particles are continuously and progressively deposited into the underlying solid rotating body. Since the smallest particles are at the base of the avalanche, they are deposited first, closer to the centre of the drum, while the largest particles at the surface of the avalanches are deposited last, closest to the drum wall.

In a circular rotating drum the particle-size segregation leads to the development of a

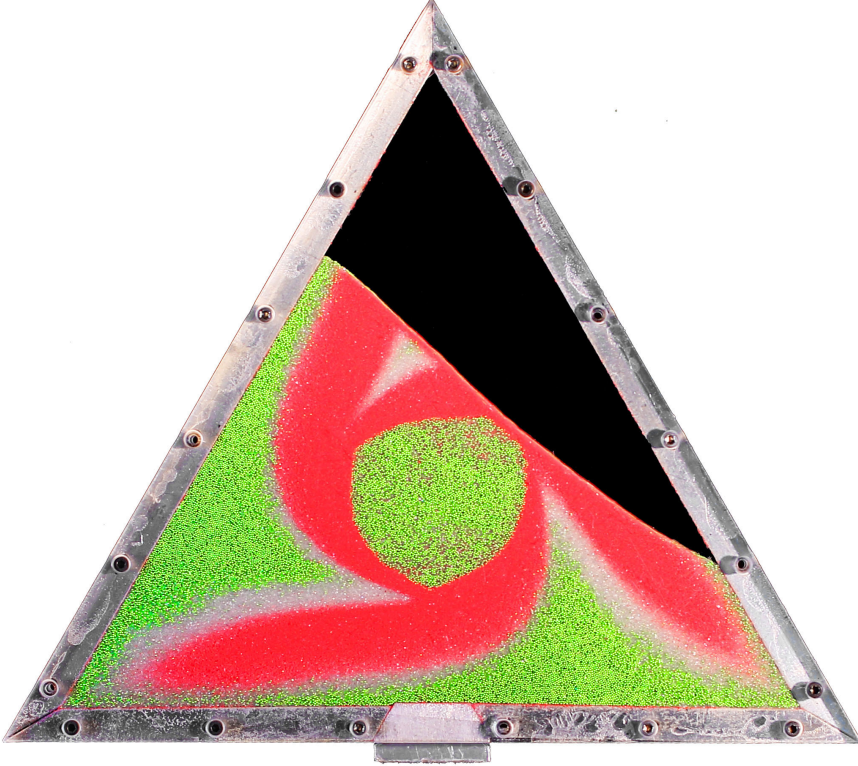


FIGURE 1: Image of a triangular rotating drum experiment 70% filled with large green ($600 - 800 \mu\text{m}$), medium white ($400 - 500 \mu\text{m}$) and small red ($125 - 160 \mu\text{m}$) glass beads in 30:40:30 mix. The drum rotates clockwise with a rotation rate of $\Omega = -\pi/48 \text{ rad/s}$. Most of the grains are in solid body rotation but a thin avalanche develops at the free surface, within which all the segregation occurs. After just two revolutions this produces a stunning quasi-periodic pattern of small and medium particle-rich arms radiating towards the corners of the drum, that are surrounded by large grains. There is also a central undisturbed core, which just rotates with the drum. Movie 1 shows the full time-dependent evolution.

radial particle-size distribution with the smallest particles concentrated in a ring around the central core and the largest grains in another ring adjacent to the drum wall (Gray & Hutter 1997; Gray & Ancey 2011). In the triangular rotating drum the particle-size distribution is considerably more complicated, but broadly speaking the largest grains are still concentrated next to the drum wall and the smallest ones are closest to the central core. However, the combination of particle-size segregation and the complex underlying bulk flow, allows a pattern to develop, with the small and medium sized particles forming arms, that are surrounded by large particles. The arms start from a position adjacent to the central core, and radiate out with a clockwise rotation to point towards the corners of the drum. This pattern forms after only two drum revolutions and is quasi-periodic, never truly settling down, but repeating in a closely similar way.

Partially filled non-circular rotating drums provide a simple example of complex granular flow with spatially and temporally evolving solid-like and liquid-like regions. Accurately modelling such flows with continuum theories is still a challenge. Barker *et al.* (2021) developed a fully-coupled theory capable of modelling both the bulk flow and the particle-size segregation. The theory is based on the incompressible $\mu(I)$ rheology for granular flows, in

which the friction μ is a function of the non-dimensional inertial number I (GDR MiDi 2004; Jop *et al.* 2006). Rather than using the classical $\mu(I)$ curve, Barker *et al.* (2021) use a modified functional form that introduces a creep state at low inertial numbers and asymptotes to a linear dependence at high inertial numbers (Barker & Gray 2017). This partially regularized form of the theory ensures that it is mathematically well-posed over a much wider range of inertial numbers than the original theory (Barker *et al.* 2015).

The inertial number $I = \dot{\gamma}d/(p/\rho_*)^{1/2}$, where $\dot{\gamma}$ is the shear rate, d is the particle size, p is the pressure and ρ_* is the intrinsic density of the grains. The fact that the rheology is locally particle-size dependent, is profound. It implies that, in general, the local flow behaviour is dependent on the evolving particle-size distribution. Modelling particle-size segregation patterns in rotating drums is therefore not necessarily just a matter of developing a theory for a monodisperse bulk flow (or parameterizing the velocity and pressure fields using the results of DEM/DPM simulations), and then solving for the particle-size segregation. In general, it is necessary to consider the feedback that the particle-size distribution has on the bulk-flow dynamics. In some flows the feedback can have a significant effect, such as in segregation-induced fingering instabilities, bulbous flow fronts, stratification patterns and petal formation in cylindrical drums (Pouliquen, Delour & Savage 1997; Pouliquen & Vallance 1999; Woodhouse *et al.* 2012; Baker, Johnson & Gray 2016*b*; Denissen *et al.* 2019; Barker *et al.* 2021; Williams 1968; Makse *et al.* 1997; Gray & Hutter 1997; Gray & Ancey 2009; Zuriguel *et al.* 2006). In other flows, the feedback can be more subtle, and prescribed fields may be sufficient to capture the main features of the segregation as well as the bulk dynamics (e.g. Wiederseiner *et al.* 2011; Schlick *et al.* 2015; Deng *et al.* 2020). The problem is that there is no way of knowing *a priori* whether the feedback in a particular flow will be significant or not.

In order to take account of segregation induced feedback on the bulk flow, this paper adopts the fully coupled framework developed by Barker *et al.* (2021). Barker *et al.* (2021) showed that this theory was able to capture the qualitative features of the segregation patterns observed in the thin square rotating drum experiments of Hill *et al.* (1999), but it over predicted the avalanche depth and under predicted its speed. The transparent front and back sidewalls (which allow observation of the patterns) impose a significant frictional force on the flow (Taberlet *et al.* 2003; Jop, Forterre & Pouliquen 2005). In particular, Jop *et al.* (2005) showed that sidewalls generate granular flows that are thinner and faster than those in wider channels. In order to make quantitative comparisons between the theory and experiments it is therefore necessary to include these side-wall friction effects into the general theory. This paper therefore makes careful quantitative comparisons between a fully coupled theory, which includes sidewall friction, and experiments in a thin triangular rotating drum.

The paper is structured as follows: In §2 the governing equations are introduced and generalized to account for sidewall friction, and §3 summarizes the numerical method. This is used in §4 to compare simulations with experiments performed in 70% filled triangular rotating drum with a 50:50 bidisperse mixture of large and small particles. The effect of the sidewalls is quantified in §5 by comparing these results with equivalent simulations performed in the absence of sidewall friction. §6 and 7 study the effect of changing the fill level and mixture composition, and §8 compares tridisperse simulations to experiments.

2. Governing equations

2.1. The partially regularised $\mu(I)$ rheology

Consider a body of granular material containing particles of differing sizes, shapes and frictional properties, but with a constant intrinsic grain density ρ_* . The solids volume fraction

151 Φ is also assumed to be constant, so that the bulk density $\rho = \Phi\rho_*$ is constant. Mass balance
 152 then implies that the bulk flow field \mathbf{u} is incompressible,

$$153 \quad \nabla \cdot \mathbf{u} = 0, \quad (2.1)$$

154 where ∇ is the gradient operator and \cdot is the dot product. Although shear and gravity-driven
 155 segregation relies on the formation of void spaces inside a flowing mixture, the bulk solids
 156 volume fraction in granular avalanches has been shown to remain approximately constant,
 157 and incompressibility is therefore a reasonable assumption (Tripathi & Khakhar 2011). The
 158 momentum balance is

$$159 \quad \rho \left(\frac{\partial \mathbf{u}}{\partial t} + \mathbf{u} \cdot \nabla \mathbf{u} \right) = -\nabla p + \nabla \cdot (2\eta \mathbf{D}) + \rho \mathbf{g}, \quad (2.2)$$

160 where p is the pressure and \mathbf{g} is the constant gravitational acceleration vector. The $\mu(I)$
 161 rheology (GDR MiDi 2004; Jop *et al.* 2006) relates the deviatoric stress to the strain-rate
 162 tensor \mathbf{D} through a granular viscosity

$$163 \quad \eta = \frac{\mu(I)p}{2\|\mathbf{D}\|}. \quad (2.3)$$

164 where the second invariant of the strain-rate tensor is

$$165 \quad \|\mathbf{D}\| = \sqrt{\frac{1}{2}\text{tr}(\mathbf{D}^2)}. \quad (2.4)$$

166 In terms of this second invariant, the inertial number becomes

$$167 \quad I = \frac{2d\|\mathbf{D}\|}{\sqrt{p/\rho_*}}, \quad (2.5)$$

168 where d is the grain diameter. The $\mu(I)$ -rheology is an empirical law which was formulated
 169 using dimensional analysis alongside evidence from DEM/DPM simulations and experiments
 170 across a range of steady-state monodisperse flow geometries (GDR MiDi 2004). Jop *et al.*
 171 (2005) derived the classical form of the $\mu(I)$ function from the basal friction measurements
 172 of Pouliquen & Forterre (2002). It took the form

$$173 \quad \mu(I) = \frac{\mu_s I_0 + \mu_d I}{I_0 + I}. \quad (2.6)$$

174 This starts at the static friction μ_s at $I = 0$ and asymptotes to the dynamic friction μ_d for large
 175 inertial numbers. The strength of the transition is controlled by the parameter I_0 . Barker *et al.*
 176 (2015) found that this formulation was well posed for inertial numbers in the range $[I_1^N, I_2^N]$
 177 provided that the $\mu_d - \mu_s$ was sufficiently large. The lower and upper neutral stability limits
 178 I_1^N and I_2^N are found by substituting (2.6) into equation (3.9) of Barker & Gray (2017) and
 179 determining the values of I for which the condition $C = 0$. When the inertial number is
 180 too low ($I < I_1^N$) or too high ($I > I_2^N$) the system leads to unbounded growth of small
 181 perturbations (ill-posedness) in the high wavenumber limit. This has been shown to lead
 182 to grid-dependent results in numerical simulations (Barker *et al.* 2015; Martin *et al.* 2017;
 183 Barker & Gray 2017), and offers an indication that important physics is missing in the model.

184 The issue of ill-posed behaviour can be resolved by the inclusion of higher gradients
 185 (Goddard & Lee 2017), non-locality (Kamrin & Koval 2012; Kamrin 2019) or compressibil-
 186 ity (Barker *et al.* 2017; Heyman *et al.* 2017; Schaeffer *et al.* 2019), but these all add further
 187 complexity to the equations. A simple, but practical, approach that retains the structure
 188 of the incompressible Navier-Stokes equations (2.1)–(2.2), is to modify the shape of the
 189 $\mu(I)$ curve to increase the theory's range of well-posedness. In the small inertial number

190 limit, Barker & Gray (2017) solved for the boundary between well- and ill-posed regions in
 191 parameter space to motivate the alternative $\mu(I)$ function

$$192 \quad \mu(I) = \begin{cases} \sqrt{\frac{\alpha}{\log\left(\frac{A}{I}\right)}}, & \text{for } I \leq I_1^N, \\ \frac{\mu_s I_0 + \mu_d I + \mu_\infty I^2}{I_0 + I}, & \text{for } I > I_1^N, \end{cases} \quad (2.7)$$

193 where $\alpha \lesssim 2$ ensures that the lower branch is well-posed for $I \in [0, I_1^N]$, μ_∞ is a new material
 194 constant and the constant

$$195 \quad A = I_1^N \exp\left(\frac{\alpha(I_0 + I_1^N)^2}{(\mu_s I_0 + \mu_d I_1^N + \mu_\infty (I_1^N)^2)^2}\right), \quad (2.8)$$

196 ensures that the function (2.7) is continuous at $I = I_1^N$. The function (2.7) implies that the
 197 friction $\mu = 0$ at $I = 0$. The partially regularised theory therefore does not have a yield
 198 stress, but instead creeps for inertial numbers $I \leq I_1^N$. This makes little practical difference
 199 to numerical simulations, which already necessitate high viscosity regularisation (see §3).

200 Since I_1^N is a lot less than unity, it follows that the upper branch of (2.7) closely
 201 approximates the original function (2.6) for $I_1^N < I \ll 1$. At large inertial numbers the
 202 upper branch asymptotes to $\mu = \mu_d + \mu_\infty I$, instead of tending to the constant value μ_d . This
 203 is consistent with the high speed chute flow experiments of Holyoake & McElwaine (2012)
 204 and Barker & Gray (2017), which showed there was a linear dependence on I at large inertial
 205 numbers. Such experiments therefore provide a means of determining the new material
 206 constant μ_∞ . Barker *et al.* (2021) showed that the creep state at small inertial numbers and
 207 the linear dependence of μ on I at large inertial numbers, significantly extends the range
 208 of well-posedness from $I = 0$ to $I \simeq 17$. It is for this reason that the theory is known as
 209 the partially-regularized $\mu(I)$ rheology, as it does not guarantee well-posedness, but instead
 210 makes the well-posed range much larger than that of the original theory (Jop *et al.* 2006;
 211 Barker *et al.* 2015).

212 2.2. Generalized polydisperse segregation theory

213 The granular material is assumed to consist of n discrete particle species ν that have differing
 214 particle diameters d^ν , but the same intrinsic grain density ρ_* . Each species has a volume
 215 fraction per unit granular volume $\phi^\nu \in [0, 1]$, which satisfies the summation constraint

$$216 \quad \sum_{\forall \nu} \phi^\nu = 1. \quad (2.9)$$

217 All of the existing bidisperse and polydisperse theories for particle-size segregation
 218 (e.g. Bridgwater, Foo & Stephens 1985; Savage & Lun 1988; Dolgunin & Ukolov 1995;
 219 Gray & Thornton 2005; Gray & Chugunov 2006; Gray & Ancey 2011; Fan & Hill 2011;
 220 Schlick *et al.* 2015; Gray 2018; Barker *et al.* 2021) can be recast in the form of general
 221 segregation-advection-diffusion equation for each species ν

$$222 \quad \frac{\partial \phi^\nu}{\partial t} + \nabla \cdot (\phi^\nu \mathbf{u}) + \nabla \cdot \mathbf{F}^\nu = \nabla \cdot \mathcal{D}^\nu, \quad (2.10)$$

223 where \mathbf{F}^ν and \mathcal{D}^ν are the segregation and diffusive flux vectors for species ν , respectively.
 224 By summing (2.10) over each species and applying the summation constraint (2.9), the

incompressibility condition (2.1) is satisfied provided

$$\sum_{\forall \nu} \mathbf{F}^\nu = \mathbf{0}, \quad \text{and} \quad \sum_{\forall \nu} \mathcal{D}^\nu = \mathbf{0}. \quad (2.11)$$

For a bidisperse mixture, the segregation flux function should satisfy the constraint that no segregation occurs when the volume fraction of either species is zero (Bridgwater *et al.* 1985). The simplest form therefore has a linear dependence on the species volume fractions, as proposed for a bidisperse mixture by Gray & Thornton (2005). This was later generalised for a polydisperse mixture (Gray & Ancy 2011; Barker *et al.* 2021) by a summation of the segregation flux functions over each bidisperse sub-mixture, to give

$$\mathbf{F}^\nu = \sum_{\forall \lambda \neq \nu} f_{\nu\lambda} \phi^\nu \phi^\lambda \mathbf{e}_{\nu\lambda}, \quad (2.12)$$

where $f_{\nu\lambda}$ is the segregation velocity magnitude and $\mathbf{e}_{\nu\lambda}$ is the unit vector along the segregation direction. This satisfies the summation constraint (2.11) provided

$$f_{\nu\lambda} = f_{\lambda\nu}, \quad \mathbf{e}_{\nu\lambda} = -\mathbf{e}_{\lambda\nu}. \quad (2.13)$$

In Barker *et al.* (2021) the diffusive flux vector is defined by analogy with the Maxwell-Stefan equations (Maxwell 1867)

$$\mathcal{D}^\nu = \sum_{\forall \lambda \neq \nu} \mathcal{D}_{\nu\lambda} \left(\phi^\lambda \nabla \phi^\nu - \phi^\nu \nabla \phi^\lambda \right), \quad (2.14)$$

so that in general the diffusion rate $\mathcal{D}_{\nu\lambda}$ may vary between sub-mixtures, while still satisfying (2.11), provided $\mathcal{D}_{\nu\lambda} = \mathcal{D}_{\lambda\nu}$. When the diffusion rate is the same across all sub-mixtures, (2.14) reduces to the standard equation for Fickian diffusion.

2.3. Segregation induced feedback on the bulk flow

The inertial number (2.5) is particle-size dependent. Hence, even if the particles have identical microscopic frictional properties, the local friction μ and hence the bulk flow behaviour will depend on the local particle size (GDR MiDi 2004). Particle-size segregation can therefore feedback on the local flow dynamics. By defining a volume fraction weighted mean particle size

$$\bar{d} = \sum_{\forall \nu} \phi^\nu d^\nu, \quad (2.15)$$

it is possible to generalize the inertial number definition (2.5) to polydisperse mixtures

$$I = \frac{2\bar{d}\|\mathbf{D}\|}{\sqrt{p/\rho_*}}, \quad (2.16)$$

This is sufficient to capture simple frictional feedback from the evolving particle-size distribution of otherwise identical particles (Rognon *et al.* 2007; Tripathi & Khakhar 2011; Denissen *et al.* 2019; Barker *et al.* 2021). This implies that for the same flow depth, small particles will flow faster than large grains, so long as nonlocal wall effects do not come into play (Pouliquen & Forterre 2002; Kamrin & Koval 2014; Edwards & Gray 2015; Edwards *et al.* 2019; Rocha *et al.* 2019).

There are more complex effects in which the frictional properties of the particles differ due to their shape and/or microscopic surface properties. For each pure phase ν , this can often be accounted for by modifying the parameters μ_s^ν , μ_d^ν , μ_∞^ν and I_0^ν in the friction law (2.7). The local effective friction of the mixture can then be defined as the volume fraction

weighted average of the constituent frictions,

$$\bar{\mu}(I) = \sum_{\forall \nu} \phi^\nu \mu^\nu(I). \quad (2.17)$$

This leads naturally to a new definition for the granular viscosity (2.3), which replaces η in the bulk momentum balance (2.2)

$$\bar{\eta} = \frac{\bar{\mu}(I)p}{2\|\mathbf{D}\|}. \quad (2.18)$$

The combination of (2.16) and (2.17) allows the frictional differences caused by variations in particle size and surface properties to feedback on the bulk motion. This is crucial for segregation-induced flow fingering, which frequently occurs in geophysical mass flows, and is responsible for longer run-out (Pouliquen *et al.* 1997; Pouliquen & Vallance 1999; Iverson & Vallance 2001; Iverson 2003; Johnson *et al.* 2012; Woodhouse *et al.* 2012; Kokelaar *et al.* 2014; Baker *et al.* 2016b; Edwards *et al.* 2023).

2.4. The feedback of the bulk flow on particle-size segregation and diffusion

Each particle species ν is transported by the bulk velocity field \mathbf{u} in the segregation-advection-diffusion equation (2.10). The particle-size distribution is therefore directly affected by the local velocity \mathbf{u} . The local shear-rate $\dot{\gamma} = 2\|\mathbf{D}\|$ and the pressure p also affect the segregation and diffusion through the functional dependence of the segregation velocity magnitude $f_{\nu\lambda}$ and diffusion rate $\mathcal{D}_{\nu\lambda}$ between each species ν and λ pair.

Barker *et al.* (2021) surveyed the existing literature for specific functional forms. In particular, dimensional analysis demands that the diffusion rate scales with the shear-rate times the particle-size squared, times an arbitrary function of the inertial number. This scaling was implied by the analysis of Scott & Bridgwater (1975) on the relationship between particle percolation velocity and diffusion, and has been extensively confirmed by experimental observations (Bridgwater 1980; Natarajan, Hunt & Taylor 1995; Utter & Behringer 2004; Katsuragi, Abate & Durian 2010) and numerical simulations (Tripathi & Khakhar 2013; Fan *et al.* 2014; Cai *et al.* 2019). The simplest model for the diffusion rate between each species ν and λ is therefore

$$\mathcal{D}_{\nu\lambda} = 2\mathcal{A}\|\mathbf{D}\|\bar{d}^2, \quad (2.19)$$

where \mathcal{A} is a universal constant specified in table 1. Note that the diffusion is therefore assumed to be the same for each species pair, and hence the diffusive flux (2.14) reduces to standard Fickian diffusion. Campbell (1997) found that diffusion in granular shear flows was anisotropic, and Utter & Behringer (2004) studied monodisperse Couette flow experiments using flat disc-shaped particles, from which they measured a radial diffusion coefficient of $\mathcal{A} = 0.108$ and a tangential diffusion coefficient of $\mathcal{A} = 0.223$. Evidence from bidisperse DEM/DPM shear-cell simulations with spherical particles implies that the anisotropy is only slight, and that instead $\mathcal{A} \in (0.03, 0.05)$ (Tripathi & Khakhar 2013; Cai *et al.* 2019; Bancroft & Johnson 2021; Artoni *et al.* 2021). Therefore isotropic diffusion can be reasonably assumed, and $\mathcal{A} = 0.04$ is used here.

Trehwela *et al.* (2021) performed single-intruder shear-box experiments to derive a scaling law for segregation of large and small particles in a bidisperse mixture. This law is now generalized to polydisperse systems. For a sub mixture composed of particles ν and λ the segregation velocity magnitude

$$f_{\nu\lambda} = \left(\frac{2\mathcal{B}\rho_*g\|\mathbf{D}\|\bar{d}^2}{C\rho_*g\bar{d} + p} \right) \mathcal{F}_{\nu\lambda}(\phi^\nu, \phi^\lambda, R_{\nu\lambda}), \quad (2.20)$$

$$\begin{aligned} \mathcal{A} &= 0.04, & \mathcal{B} &= 0.7125, & C &= 0.2712, \\ \mathcal{E} &= 2.0957, & a &= 9 & \phi_c^s &= 0.2. \end{aligned}$$

TABLE 1: Parameter values used in the numerical simulations. The value of the universal constant \mathcal{A} in the diffusivity (2.19) is based on the DEM/PDM simulations of (Tripathi & Khakhar 2013; Cai *et al.* 2019; Bancroft & Johnson 2021; Artoni *et al.* 2021). The values of the universal constants \mathcal{B} and C in the segregation law (2.20) are based on those suggested by the single intruder experiments of Trewhela *et al.* (2021), although \mathcal{B} is corrected for the absence of an interstitial fluid. The remaining non-dimensional constants \mathcal{E} , a and ϕ_c^s are also taken from Trewhela *et al.* (2021).

where \mathcal{B} and C are universal constants determined by Trewhela *et al.* (2021) (given in table 1). The function $\mathcal{F}_{\nu\lambda}$ accounts for packing effects and the segregation-rate dependence on the generalized grain-size ratio

$$R_{\nu\lambda} = \max\left(\frac{d^\nu}{d^\lambda}, \frac{d^\lambda}{d^\nu}\right), \quad (2.21)$$

where $R_{\nu\lambda} = R_{\lambda\nu} > 1$. The scaling law (2.20) is able to capture a variety of phenomena observed in slightly dilated, bidisperse, sheared granular flows, where kinetic sieving and squeeze expulsion are the dominant segregation mechanisms (Middleton 1970; Bridgwater *et al.* 1985; Savage & Lun 1988; Gray 2018).

Kinetic sieving is a shear driven process that allows smaller particles to percolate down under the action of gravity, while squeeze expulsion describes the process in which particles are squeezed upwards to maintain bulk incompressibility. Dimensional analysis suggests that the segregation rate should have the dimensions of a velocity, and (2.20) assumes that $f_{\nu\lambda}$ behaves like $\dot{\gamma}\vec{d} = 2||\mathbf{D}||\vec{d}$, which automatically implies that the segregation flux function $f_{\nu\lambda}\phi^\nu\phi^\lambda$ is asymmetric (van der Vaart *et al.* 2015; Gajjar & Gray 2014). By performing experiments with a density matched interstitial fluid, Vallance & Savage (2000) showed that segregation shuts off in the absence of gravity (see also Thornton, Gray & Hogg 2006). The effect of gravity is included indirectly in the round bracketed term in (2.20) through a dependence on the reciprocal of the non-dimensionalized pressure $p/(\rho_*g\vec{d})$. If the shear rate is constant, this form implies that the deeper one goes into the mixture the lower the segregation rate becomes. This was observed directly in Trewhela *et al.*'s (2021) experiments, i.e., the intruders did not rise linearly with time in response to a spatially uniform shear rate, but were either percolated down or squeezed up faster near the free surface. The constant C in (2.20) was included to avoid a singularity at zero pressure. Further evidence of the pressure dependence of segregation is provided in the papers of Golick & Daniels (2009), Fry *et al.* (2018) and Bancroft & Johnson (2021).

Trewhela *et al.* (2021) found that for moderate grain-size ratios of large and small particles (i.e. for $R_{sl} \in [1, 4.17]$, where s and l denote small and large particles, respectively), the segregation rate of large intruders had a linear dependence on $(R_{sl} - 1)$. However, the segregation rate of a small intruder obeyed a quadratic law of the form $(R_{sl} - 1) + \mathcal{E}(R_{sl} - 1)^2$, where \mathcal{E} was a non-dimensional constant. The additional quadratic dependence arose because small intruders find it increasingly easy to percolate through a matrix of large grains as the particle-size ratio approaches the spontaneous percolation limit at around $R_{sl} \simeq 6$. Trewhela *et al.* (2021) extended their model to intermediate concentrations by assuming that

$$\mathcal{F}_{sl} = (R_{sl} - 1) + \mathcal{E}\Lambda(\phi^s)(R_{sl} - 1)^2, \quad (2.22)$$

where the function

$$\Lambda(\phi^s) = \begin{cases} 1 - \frac{\phi^s}{\phi_c^s}, & \text{for } \phi^s \leq \phi_c^s, \\ 0, & \text{for } \phi^s > \phi_c^s, \end{cases} \quad (2.23)$$

gives the right \mathcal{F}_{sl} dependence in the limit as $\phi^s \rightarrow 0, 1$ and shuts off the quadratic dependence when the small-particle concentration exceeds ϕ_c^s (defined in table 1). Trewhela *et al.* (2021) showed that this functional form was capable of quantitatively capturing the spatial and temporal evolution of the particle-size distribution measured in the refractive-index-matched shear-box experiments of van der Vaart *et al.* (2015).

However, there is evidence from experiments and DEM/DPM simulations suggesting that for 50:50 mixtures of large and small particles in geometries for which the velocity and shear-rate are functions of space and time, the segregation intensity is maximal near a grain-size ratio of $R_{sl} = 2$ (Golick & Daniels 2009; Thornton *et al.* 2012), whereas the formulation (2.22) is monotonically increasing with the size ratio. Trewhela *et al.* (2021) therefore suggested an alternative size-ratio dependency which captures this effect, within the framework of incompressible segregation theory

$$\mathcal{F}_{sl} = \frac{(R_{sl} - 1) + \varepsilon \Lambda(\phi^s)(R_{sl} - 1)^2}{1 + a(R_{sl} - 1)^2 \phi^s \phi^l}, \quad (2.24)$$

where a is a constant defined in table 1. The numerator in (2.24) is the same as (2.22), but the denominator now includes a reduction factor $1 + a(R_{sl} - 1)^2 \phi^s \phi^l$, which shuts off when $\phi^s = 0$ and $\phi^l = 0$, and reduces the segregation rate at intermediate configurations. The idea is that this factor parameterizes the enhanced packing of mixtures of particles of different sizes, which is thought to reduce the segregation rate. Trewhela *et al.* (2021) showed that for a 50:50 mix, equation (2.24) predicts a peak segregation rate at $R_{sl} \simeq 1.66$, which is very close to the maximum at $R_{sl} = 1.7$ observed in the DEM/DPM simulations of Thornton *et al.* (2012). The bidisperse simulations in §§4–7 of this paper are performed using the functional form (2.24). Almost nothing is known about how the segregation rate and the packing behaves in polydisperse sheared granular mixtures. The tridisperse simulations presented in §8 therefore use a trivial pairwise generalization of (2.24) as an illustration.

2.5. Sidewall friction

It has long been known that confining lateral sidewalls play an important role in granular flow experiments (Greve & Hutter 1993; Taberlet *et al.* 2003; Jop *et al.* 2005; Baker, Barker & Gray 2016a). In rotating drum flows the additional friction introduced by sidewalls results in avalanches which are significantly thinner and faster than flows without sidewall friction (Hill *et al.* 1999; Ottino & Khakhar 2000; Jop *et al.* 2005; Mouny 2007). As a result, the two-dimensional square rotating drum simulations of Barker *et al.* (2021) could not be compared directly to experiments. In principle, a Coulomb friction boundary condition could be imposed on the sidewalls and then the governing equations could be solved in three dimensions for any width of drum. However, the fact that the avalanche is so thin, implies that high resolution numerical simulations are required to adequately resolve the velocity profile and segregation, which makes this approach very computationally expensive. In this paper the influence of sidewall friction is therefore incorporated into the governing equations by width averaging the momentum balance equation (2.2). This reduces the problem to a two dimensional one, which is much more computationally efficient.

Consider then a three-dimensional granular flow confined within a narrow channel between $y = 0$ and $y = W$, where there can be slip at the side walls and only weak velocity gradients in the y -direction. Proceeding in a similar manner to Jop *et al.* (2005), assuming a Coulomb

friction boundary condition at the lateral sidewalls implies

$$\boldsymbol{\tau} \cdot \mathbf{n} = -\mu_W p \frac{\mathbf{u}}{|\mathbf{u}|} \quad \text{at } y = 0, W, \quad (2.25)$$

where \mathbf{n} is an outward pointing normal to the sidewall, μ_W is a constant wall friction coefficient and the term $-\mathbf{u}/|\mathbf{u}|$ ensures that friction acts against the flow. The three-dimensional mass and momentum balance equations, defined analogously with (2.1) and (2.2), may then be integrated across the channel width in a similar fashion to the depth-averaged approach for a shallow system (Gray 2001; Gray & Edwards 2014). Width-integrated variables are defined by

$$\tilde{f} = \frac{1}{W} \int_0^W f dy, \quad (2.26)$$

for any variable f , and when variations in the y -direction are small, $\widetilde{fg} \simeq \tilde{f}\tilde{g}$ for any two variables f and g . Integrating and applying the boundary conditions (2.25) results in a two-dimensional system for which the mass and momentum balances become

$$\boldsymbol{\nabla} \cdot \tilde{\mathbf{u}} = 0, \quad (2.27)$$

$$\rho \left(\frac{\partial \tilde{\mathbf{u}}}{\partial t} + \tilde{\mathbf{u}} \cdot \boldsymbol{\nabla} \tilde{\mathbf{u}} \right) = -\boldsymbol{\nabla} \tilde{p} + \boldsymbol{\nabla} \cdot (2\tilde{\eta} \tilde{\mathbf{D}}) + \rho \mathbf{g} - \frac{2}{W} \mu_W p \frac{\tilde{\mathbf{u}}}{|\tilde{\mathbf{u}}|}, \quad (2.28)$$

where $\boldsymbol{\nabla} = (\partial/\partial x, \partial/\partial z)^T$, the two-dimensional gradient operator. Since there is no lateral flow and small velocity gradients in the y -direction, $\mathbf{u}/|\mathbf{u}| \simeq \tilde{\mathbf{u}}/|\tilde{\mathbf{u}}|$, and the tilde notation may be dropped on the understanding that the variables (\mathbf{u} , p , η , \mathbf{D}) from this point onwards refer to width-averaged quantities of the form (2.26). The final term in the momentum balance equation (2.28) models the influence of sidewall friction on the bulk flow. This alteration provides a straightforward method of capturing three-dimensional wall friction effects in a two-dimensional framework.

3. Numerical method

The mass (2.27) and momentum balances (2.28) are solved in conservative form,

$$\boldsymbol{\nabla} \cdot \mathbf{u} = 0, \quad (3.1)$$

$$\frac{\partial}{\partial t} (\varrho \mathbf{u}) + \boldsymbol{\nabla} \cdot (\varrho \mathbf{u} \otimes \mathbf{u}) = -\boldsymbol{\nabla} p + \boldsymbol{\nabla} \cdot (2\eta \mathbf{D}) + \varrho \mathbf{g} - \frac{2}{W} \mu_W p \frac{\mathbf{u}}{|\mathbf{u}|}, \quad (3.2)$$

where ϱ is the mixture density and \otimes is the dyadic product. In order to handle the evolving free-surface, Barker *et al.* (2021) used a two-fluid approach in which an excess air phase was considered in addition to the grains. As a result the governing equations can be numerically solved in a fixed domain, rather than using a deformable grid that adjusts to the evolving free surface, or a particle based numerical method, i.e. Smooth Particle Hydrodynamics (SPH) or the Material Point Method (MPM). The solids volume fraction Φ , remains unchanged throughout the mixture, with the excess air considered separately to the background interstitial air, which has volume fraction $1 - \Phi$ per unit mixture volume. For a bidisperse granular mixture of small and large particles with excess air, there are volume fractions φ^s , φ^l and φ^a respectively. The mixture density ϱ and viscosity η are therefore defined as volume fraction weighted averages including the excess air phase

$$\varrho = \sum_{\forall \nu} \varphi^\nu \varrho^\nu, \quad \eta = \sum_{\forall \nu} \varphi^\nu \eta^\nu. \quad (3.3)$$

$\mu_s = \tan(22^\circ)$	$\mu_d = \tan(34^\circ)$	$I_0 = 0.249$	$\mu_\infty = 0.04$
$\alpha = 1.9$	$I_1^N = 0.02048$	$\rho_* = 2500 \text{ kg/m}^3$	$\Phi = 0.6$
$d^s = 0.35 \times 10^{-3} \text{ m}$	$d^l = 0.7 \times 10^{-3} \text{ m}$	$R_{sl} = 2$	$\mathbf{e} = -\mathbf{g}/ \mathbf{g} $
$\varrho^a = 1 \text{ kg/m}^3$	$\eta^a = 10^{-3} \text{ kg/(ms)}$	$f_{ag} = 5 \text{ m/s}$	$\mathcal{D}_{al} = \mathcal{D}_{al} = 0 \text{ m}^2/\text{s}$
$\mu_W = \tan(15.5^\circ)$	$W = 3 \times 10^{-3} \text{ m}$		

TABLE 2: Parameters for the large and small glass beads, the air phase and the triangular drum. The physical parameters for glass beads are adapted from those used by Rocha *et al.* (2019) and Mangeney *et al.* (2007), to model the experiments of Félix & Thomas (2004). These parameters are used to determine I_0 using the definition given by Jop *et al.* (2005), and μ_∞ is chosen to ensure a well-posed partially-regularised $\mu(I)$ curve up to $I = 17.0189$.

The density of air ϱ^a is a constant, and $\varrho^g = \Phi \rho_* \gg \varrho^a$, where the superscript g denotes the granular phase. The granular viscosities η^g are derived from (2.18) and the viscosity of air η^a is assumed to be constant. All the relevant numerical parameters are specified in table 2. The excess air is assumed to be of sufficiently low density and viscosity that it does not affect the motion of the grains, and is purely a numerical convenience.

The two-fluid approach uses the counter-gradient transport method (Rusche 2002; Weller 2008) to sharpen the air-grain interface. This can lead to grid-dependent bubbles of excess air becoming trapped within the high viscosity granular matrix (Barker *et al.* 2021). In order to remove these bubbles, Barker *et al.* (2021) used the advection-segregation-diffusion equations (2.10) to rapidly expel the excess air from the grains. Instead of solving a bidisperse segregation problem, Barker *et al.* (2021) therefore solved a three-phase segregation problem. The segregation of both the grains and the excess air was assumed to align with gravity, and it was assumed that air-grain diffusion was zero. This implies that the advection-segregation-diffusion equation (2.10) produces a system of three conservation laws

$$\frac{\partial \varphi^l}{\partial t} + \nabla \cdot (\varphi^l \mathbf{u}) + \nabla \cdot \left(-f_{ls} \varphi^l \varphi^s \frac{\mathbf{g}}{|\mathbf{g}|} + f_{ag} \varphi^l \varphi^a \frac{\mathbf{g}}{|\mathbf{g}|} \right) = \nabla \cdot \left(\mathcal{D}_{ls} (\varphi^s \nabla \varphi^l - \varphi^l \nabla \varphi^s) \right), \quad (3.4)$$

$$\frac{\partial \varphi^s}{\partial t} + \nabla \cdot (\varphi^s \mathbf{u}) + \nabla \cdot \left(f_{sl} \varphi^s \varphi^l \frac{\mathbf{g}}{|\mathbf{g}|} + f_{ag} \varphi^s \varphi^a \frac{\mathbf{g}}{|\mathbf{g}|} \right) = \nabla \cdot \left(\mathcal{D}_{sl} (\varphi^l \nabla \varphi^s - \varphi^s \nabla \varphi^l) \right), \quad (3.5)$$

$$\frac{\partial \varphi^a}{\partial t} + \nabla \cdot (\varphi^a \mathbf{u}) + \nabla \cdot \left(-f_{ag} \varphi^a \varphi^g \frac{\mathbf{g}}{|\mathbf{g}|} \right) = 0, \quad (3.6)$$

where the overall concentration of grains is

$$\varphi^g = \varphi^s + \varphi^l = 1 - \varphi^a. \quad (3.7)$$

The granular segregation velocity magnitude f_{sl} is defined by the scaling law (2.20) with \mathcal{F}_{sl} given by (2.24), and $f_{ag} = f_{as} = f_{al}$ assumed to equal a sufficiently large constant (defined in table 2) to expel the excess air rapidly from the grains. The sum of equations (3.4)–(3.6) reduces to the bulk incompressibility relation (3.1). Moreover, when there is no excess air $\varphi^a = 0$, they reduce to the bidisperse advection-segregation-diffusion equations (Gray & Chugunov 2006; Gray 2018).

Equations (3.1)–(3.2) are of the form of the incompressible Navier–Stokes equations and the pressure-velocity coupling is solved by the PISO algorithm in OpenFOAM (Issa 1986), while the concentration equations (3.4)–(3.6) are solved using the Multidimensional Universal Limiter for Explicit Solution (MULES) algorithm (Weller 2006). The velocity solution and coupling to the mixture composition are calculated explicitly, leading to a Courant–Friedrichs–Lewy (CFL) criterion incorporating the local viscosity

452 (Moukalled, Mangani & Darwish 2016), where the CFL number is defined as

$$453 \quad \text{CFL} = \frac{|\mathbf{u}| \Delta t}{\Delta x} + \frac{\eta \Delta t}{\rho \Delta x^2}. \quad (3.8)$$

454 This should be limited to a characteristic value for the time integration scheme (such as
 455 unity for forward Euler). In most multi-phase flows the convective term dominates and
 456 the second, viscous term is neglected. The reverse is true for static granular material as
 457 the strain-rate tends to zero and the viscosity thus becomes infinite, with the resulting
 458 requirement that time steps become infinitesimally small. To avoid infinitesimal time steps, a
 459 high, constant cut-off value η_{\max} is used for the viscosity (see e.g. Lagr  e, Staron & Popinet
 460 2011; Staron, Lagr  e & Popinet 2012), which is redefined as

$$461 \quad \eta = \min(\eta_{\max}, \eta). \quad (3.9)$$

462 This means that a Newtonian viscosity is activated as $\|\mathbf{D}\| \rightarrow 0$ or $p \rightarrow \infty$. Smaller time steps
 463 are nevertheless required relative to low viscosity simulations as the viscosity continues to
 464 dominate the CFL number. Finally, since the partially regularised $\mu(I)$ -rheology (2.7) does
 465 not have a yield stress and instead enters a creep regime for small values of the inertial
 466 number to maintain well-posedness (Barker & Gray 2017), it is not able to model static
 467 material, as detailed in §2.1. It is important to note that although the $\mu(I)$ -rheology of
 468 Jop *et al.* (2005) does have a yield stress, the maximum viscosity cutoff (3.9) introduces
 469 a creep state numerically. This is, however, not sufficient to guarantee well posedness of
 470 the equations (Barker *et al.* 2015; Martin *et al.* 2017; Barker & Gray 2017). The partially
 471 regularized theory of Barker & Gray (2017), used here, is therefore strongly preferable
 472 due its significantly extended region of well-posedness. The numerical method has been
 473 extensively tested by Barker *et al.* (2021), and the influence of wall friction term is further
 474 tested in appendix A against a semi-infinite shear-box solution between lateral side walls.

475 4. Segregation and flow of a bidisperse mixture in a triangular rotating drum

476 4.1. Experimental set-up

477 Experiments were conducted in a triangular rotating drum with equilateral sides of length
 478 $L = 0.257$ m. This was formed from an aluminium outer frame that was confined between
 479 two transparent Polymethyl Methacrylate (PMMA) plates (separated by a gap of width
 480 $W = 3 \times 10^{-3}$ m) and screwed together. Before assembly, the PMMA walls were cleaned
 481 with anti-static spray and dried to prevent smaller particles sticking to the sidewalls. The
 482 glass beads used in the experiments were sourced from Sigmund Lindner GmbH. The larger
 483 green glass beads were sieved to a diameter $d^l = 600 - 800 \mu\text{m}$, while the smaller red
 484 beads had a diameter $d^s = 300 - 400 \mu\text{m}$. The desired volumes of large and small grains
 485 were measured separately, mixed together and then filled into the drum through a gap in
 486 the aluminium frame, which was then tightly closed with a stopper. The exact volume of
 487 grains in the drum can vary slightly from the individual combined large and small volumes
 488 due to enhanced packing of the mixture (Golick & Daniels 2009; Thornton *et al.* 2012). If
 489 necessary, additional grains were added to obtain the desired fill. For the particle-size ratios
 490 used in this paper these packing effects were small, and the theory, which is incompressible,
 491 appears to be able to capture the observed dynamics and the segregation patterns to a high
 492 degree of accuracy.

493 Particles of different sizes have a strong propensity to segregate. In order to obtain an
 494 approximately homogenous initial condition, the drum was oriented horizontally and shaken
 495 to induce segregation in the direction normal to the lateral transparent sidewalls. The large

green beads therefore segregated to the front (observable) wall, with the small red beads concealed behind them against the rear wall. At any given cross section of the drum an approximately uniform initial mixture of large and small particles was generated. The back of the drum was then attached to an ElectroCraft S642-1B/T stepper motor and a modulation speed control unit to control the rotation rate. The axis of rotation coincided with the centre of the triangle. The drum was narrow enough that cross-slope particle diffusion, within the flowing avalanche, was sufficient to smooth out any lateral variation across it. The final pattern was therefore approximately uniform across the gap, except in the central core, which never entered the avalanche. This initial condition therefore has the additional advantage that the undisturbed core appears to the observer from the front as a uniform region of green particles, providing a strong contrast with the predominantly small red particles that are deposited adjacent to the core. The sidewall friction $\mu_w = \tan(15.5^\circ)$ is a material property of both the glass beads and the PMMA, and is measured empirically from the angle of failure for a bidisperse mixture of static grains on a gradually inclined PMMA surface (see table 2).

Figure 2 shows a series of photographs of the evolving pattern that develops when a 50:50 bidisperse mixture of large and small grains is rotated in a 70% filled triangular drum rotating at 2.5 rpm. Movie 2 shows the full time-dependent evolution. The granular free surface, which was initially horizontal, inclines until a critical angle is exceeded, and a thin surface avalanche forms. The particles segregate very efficiently from one another in the surface avalanche, with the large particles rising to the surface and the small particle percolating down to the base, where they are first to deposit into the underlying solid rotating body of grains. As a result the large green grains end up adjacent to the drum wall and the smaller red particles deposit closer to the central core. The complex flow field allows a quasi-periodic pattern to develop after just two rotations, which has small particle rich arms that radiate outwards and point towards the corners of the triangle. A full discussion of the experimental results is deferred until the particle-size distribution of the numerical simulation is introduced in §4.4.

4.2. Coordinate system, boundary and initial conditions for the simulations

In order to simulate the segregation of the grains in the experimental rotating drum, a fixed Cartesian coordinate system Oxz is defined with the origin O at the axis of rotation and the z coordinate pointing in the opposite direction to gravity. The large and small particle diameters are assumed to take average values $d^l = 700 \mu\text{m}$ and $d^s = 350 \mu\text{m}$. The large particles are therefore twice the size of the small grains. The drum is filled to 70% of its volume with an initially homogeneous 50:50 mixture of large and small grains, so that $\varphi^s = \varphi^l = 0.5$ everywhere within the granular material. In addition at $t = 0$ all the material is assumed to be in solid body rotation with velocity

$$\mathbf{u} = \Omega r \boldsymbol{\theta}, \quad (4.1)$$

where Ω is the rotation rate, r is the radial coordinate and $\boldsymbol{\theta}$ is the azimuthal unit vector (Gray 2001). A rotation rate of 2.5 rpm ($\Omega = -\pi/12$ rad/s) is imposed, which places the drum in the rolling, or continuously avalanching, regime (Henein *et al.* 1983; Rajchenbach 1990; Gray 2001; Mellmann 2001; Ding *et al.* 2002; Yang *et al.* 2008). This implies that when the slope exceeds a critical angle, a liquid-like free-surface avalanche forms that continuously erodes and deposits grains with an underlying solid rotating granular body beneath.

It is useful to define the relative velocity to the drum as

$$\hat{\mathbf{u}} = \mathbf{u} - \Omega r \boldsymbol{\theta}. \quad (4.2)$$

No-slip and no-penetration conditions are imposed on the triangular walls which, using the relative velocity, can be expressed as $\hat{\mathbf{u}} = \mathbf{0}$ on the drum walls. These conditions are applied on the rotating mesh using OpenFOAM's mesh-motion routines, with a structured triangular

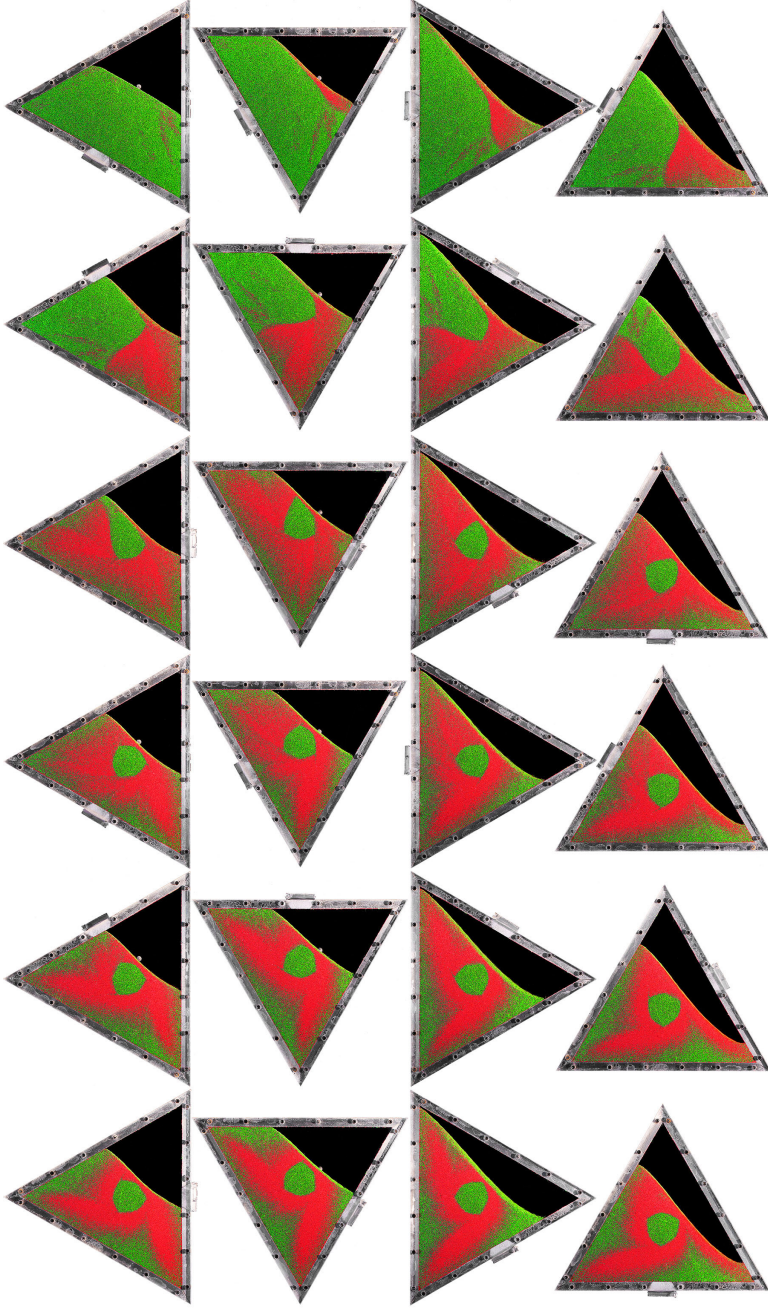


FIGURE 2: Experimental photos of a 70% filled drum with a 50:50 mixture of large green ($d^l = 600 - 800 \mu\text{m}$) and small red ($d^s = 300 - 400 \mu\text{m}$) glass beads rotating at 2.5 rpm. Solid body rotation occurs in the first 2 seconds. The sequence starts at $t = 2 \text{ s}$ and progresses in increments of 2 s (30° rotation), from left to right, top to bottom, up to $t = 48 \text{ s}$ (2 revolutions). Once the surface avalanche develops, the mixture gradually segregates into a structure of small particle arms. The protruding stopper provides a reference point for the rotation. Movie 2 shows the full time-dependent evolution and is available in the online supplementary material.

mesh containing $N^2 = 600^2$ cells. The parameters for segregation and diffusion are the universal constants summarized in table 1, while the frictional and remaining parameters for the glass beads and sidewall friction are specified in table 2. There are therefore no fitting parameters used in the simulations.

4.3. Bulk flow solutions and comparison to experiments

In the experiments and numerical simulations, the granular free surface is initially horizontal. As the drum rotates the granular material performs solid body rotation until a critical angle is reached, and a liquid-like avalanche develops adjacent to the free surface. Due to sidewall friction, the critical free-surface inclination is significantly higher than the static friction angle $\zeta_s = \tan^{-1}(\mu_s)$, which is usually the approximate angle of failure (Barker *et al.* 2021). The free-surface inclination remains relatively constant, with only subtle periodic variations as shown in figure 3 and movies 3–5. The entire flow then exhibits a quasi-periodic pulsating behaviour every 120° of rotation (8 s), due to the rotation of the drum and the continuously changing drum cross section occupied by the grains.

There can be subtle feedback effects from the evolving grain-size distribution, but they are not large at 70% fill (Hill *et al.* 1999; Mounty 2007). The simulation reproduces very closely the free-surface inclination observed experimentally (figure 2), including the slight S-shape, which becomes more pronounced when the free-surface is longest, and the subtle inclination dip (at $t = 42$ s in figure 3), which occurs just past the halfway point of the avalanche. Feedback between the bulk flow and the mixture composition plays a more pivotal role at fill levels near 50%, when the strongly composition-dependent velocity field can lead to the formation of petal-like patterns in the particle distribution (Zuriguel *et al.* 2006) for circular drums, and more complex patterns in triangular and square drums (Hill *et al.* 1999; Khakhar *et al.* 1999; Ottino & Khakhar 2000; Mounty 2007).

The length of the avalanche depends on the orientation of the drum. The orientations that generate the longest avalanches, also produce the deepest and fastest flowing motion (see times $t = 46$ and 48 s in figure 3a). The longer avalanche length means that more particles are entrained into the avalanche, which increases the flux and the peak velocities that occur about halfway down the avalanche. In the lower reach of the avalanche the particles are deposited back into the solid rotating body and the avalanche thins and decelerates. The super inclination of the slope, combined with acceleration down the increased avalanche length, may also contribute to the peak velocity.

The active avalanching layer is very thin, and is close to the depth observed in the experiments shown in figure 2 and movie 2. Below the avalanching layer the relative velocity $\hat{\mathbf{u}}$ rapidly decays into a quasi-static creep state. The pressure (figure 3b) has a lithostatic component, but with increasing depth the pressure gradient becomes increasingly gravity aligned. Since both the segregation velocity magnitude and the inertial number are strain-rate dependent, the inertial number (figure 3c) gives an accurate identification of the active layer in which segregation takes place. It appears slightly deeper than that implied by figure 3(a) since $\log_{10}(I)$ is plotted. It exhibits less variation in magnitude than $|\hat{\mathbf{u}}|$ and p with changing orientation, in part due to the chosen logarithmic scale, but also because the strain-rate dependent inertial number is tied to velocity gradients rather than velocity. The white dashed line in figure 3(c) indicates the threshold for the high viscosity cutoff (3.9). Above the white dashed line the dynamic and creep regimes of the partially regularized rheology (2.7) are active, while below it the high Newtonian viscosity is applied. Since this quasi-static creeping region is predominantly in rigid body rotation, it has little influence on the overall flow dynamics.

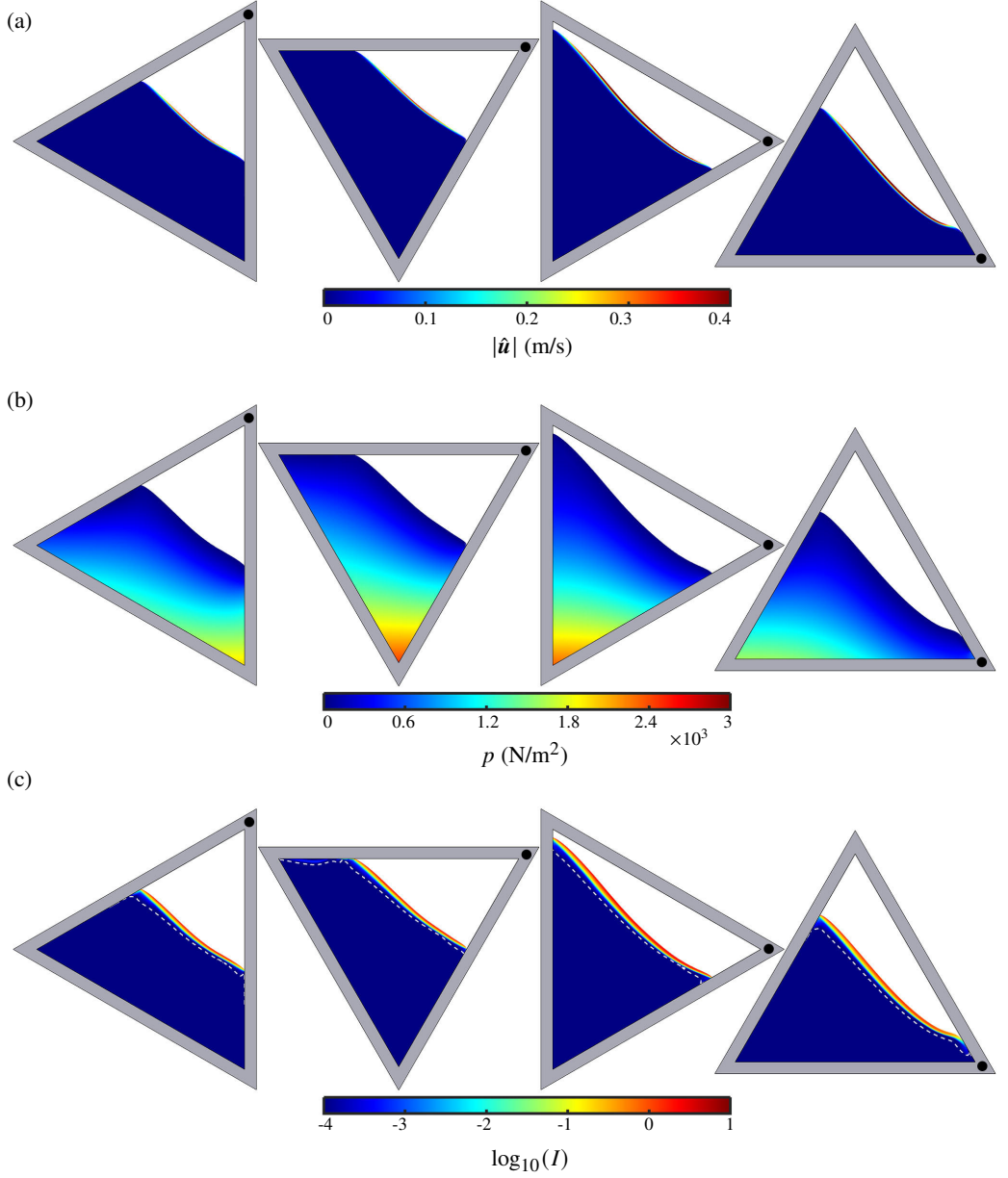


FIGURE 3: Quasi-periodic motion repeating every 120° of revolution for a 70% full triangular drum computed using the parameters from tables 1 and 2. For illustration each field is shown at $t = 42, 44, 46$ and 48 s, from left to right, corresponding to one third of a revolution. A black dot is plotted on one corner of the drum frame so that the changing orientation may be easily tracked. Panel (a) shows the modulus of the relative velocity field, (b) the pressure, and (c) the base 10 logarithm of the inertial number. The white dashed line in (c) represents the position below which the high viscosity cut-off (3.9) becomes active. The full time-dependent evolution of each of the fields is shown movies 3–5 (available online).

4.4. Particle-size distribution

Figure 4 shows a sequence of images of the computed time-dependent evolution of the small-particle concentration in the 70% filled drum with a 50:50 mix of large and small particles. Each image is directly comparable to the experimental photos in figure 2, and is separated by two seconds, or equivalently 30° angular increments, beginning at $t = 2$ s and ending after two revolutions. Movie 6 shows the full time-dependent evolution. In regions of solid-body-like rotation, the shear rate is very close to zero, so the scaling laws, (2.19) and (2.20) imply that both the diffusion and the segregation are negligibly small. The grains therefore stay at $\varphi^s = 0.5$ during their initial phase of rotation. The surface avalanche is, however, very efficient at segregating differently sized particles, because the shear rate is high and the pressure is low. This implies that the segregation velocity magnitude (2.20) is much higher than in the solid rotating body, and the grains can segregate. As the particles are deposited along the lower reach of the avalanche into the solid rotating body of grains beneath, the segregation rate once again shuts off, and the deposited particle-size distribution is rotated with the drum. The active region of segregation is therefore confined to a narrow boundary layer close to the free surface, i.e. the avalanche. The highest rate of segregation occurs adjacent to the free surface, as observed experimentally here (see §4.5) and elsewhere (Gray & Hutter 1997; Khakhar, McCarthy & Ottino 1997). This effect is intensified by the fact that particles near the free surface have longer trajectories through the actively segregating layer before being deposited, and hence are subject to more accumulated shear.

Since the fill level of the drum exceeds 50%, a central core forms that is never entrained into the avalanche and remains at its initial concentration (Gray 2001; Mounty 2007). The central core is a three-sided shape with curved sides, reminiscent of a Reuleaux triangle. The size of the core is in good agreement with the experiment (figure 2), which is a direct result of (i) the sidewall friction making the avalanche thinner and faster than equivalent flows without sidewall friction, and (ii) the segregation (2.20) and diffusion (2.19) laws confining the particle redistribution to the avalanching region. In contrast, in Barker *et al.*'s (2021) simulations (which neglected sidewall friction) the avalanche was deeper and slower, and consequently both the central core size and the segregation were underestimated compared to experimental observations (Hill *et al.* 1999; Ottino & Khakhar 2000; Mounty 2007).

Over the first full rotation, the material separates out around the homogeneous core into distinct regions of predominantly large or small particles with a diffuse region separating them. The larger particles, that segregate to the surface of the avalanche, deposit close to the drum wall, while the smaller particles at the base of the avalanche, deposit adjacent to the central core. The combination of the complex time-dependent bulk flow (described in §4.3) and the ordering mechanism of particle-size segregation, then begins to generate a pattern which has small-particle-rich arms. The first arm emerges after one complete rotation of the drum (figure 4), and the second arm then follows one third of a turn later. The timescale for the gradual formation of the pattern is captured by the numerical simulation, as shown by the excellent frame-by-frame match between figures 2 and 4, and movie 7. Over the second rotation of the drum, the arms pass through the avalanche again, the segregation becomes stronger and the pattern becomes more clearly defined. On each third of a revolution the pattern then approximately repeats. Simulations are therefore only performed for the first two drum revolutions.

The pattern exhibits a strong three-fold symmetry. To see this more clearly, it is useful to plot the $\varphi^s = 0.5$ contour, and then replot it twice more rotated by $\pm 2\pi/3$ radians. This is done in figure 5 at $t = 36$ and 44 s. In both cases this produces a triskelion-like pattern with three arms that start adjacent to the central core and radiate outwards in a clockwise sense ultimately pointing towards the corners of the drum. The outer length of the arm is roughly

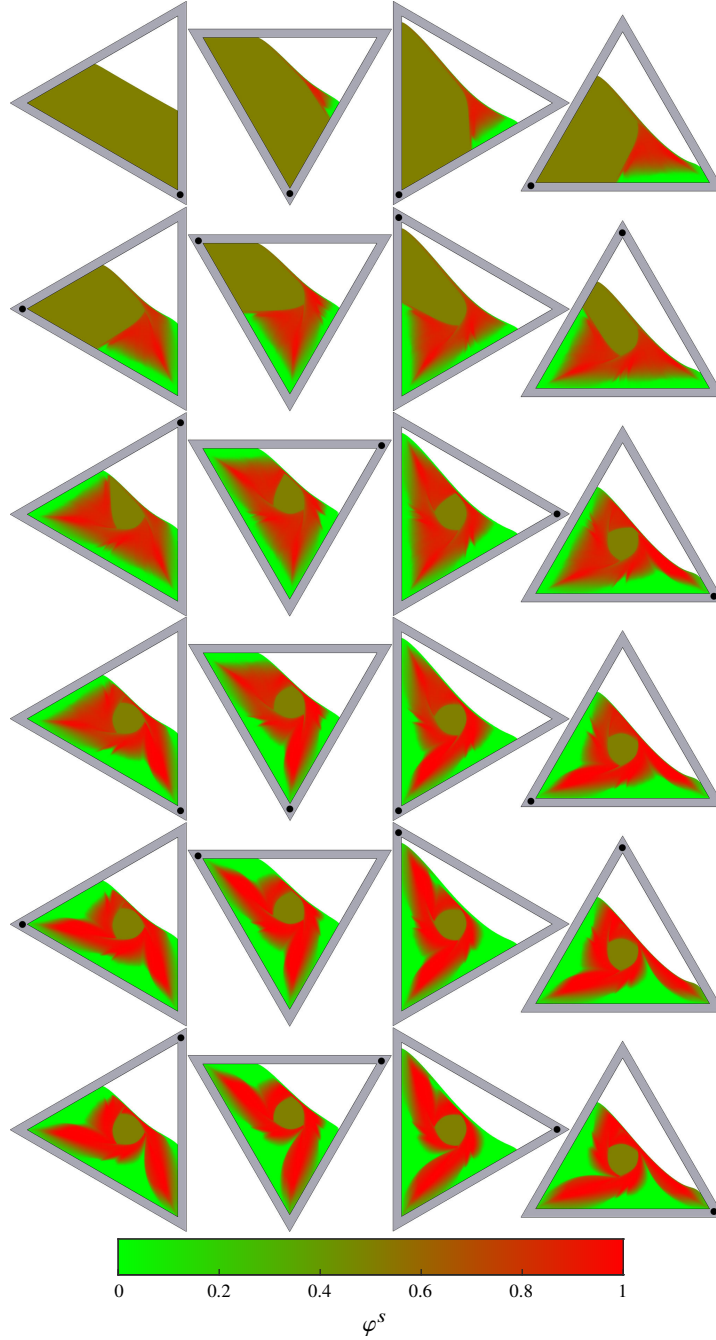


FIGURE 4: Small-particle concentration in a 70% filled triangular rotating drum with a 50:50 mixture of large and small particles, computed using the parameters specified in tables 1 and 2. The simulation is shown over two full revolutions, beginning at $t = 2$ s and progressing in increments of 2 s, or 30° angular increments, from left to right, top to bottom. The excess air above the grains is coloured white. The images are directly comparable to the experimental photos in figure 2. A small black dot in one corner of the triangular frame provides a reference point for the clockwise rotation. Movie 6 shows the full time-dependent evolution, and this is compared side-by-side to the experiment in movie 7.

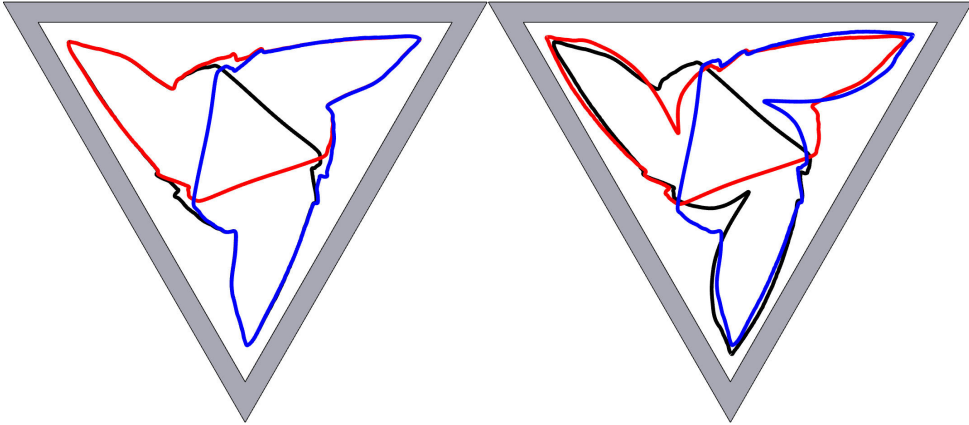


FIGURE 5: The rotational symmetry of the small particle rich arms is shown by plotting the $\varphi^s = 0.5$ contour for the numerical simulations of a 70% filled triangular rotating drum containing a 50:50 bidisperse mixture at $t = 36$ s (left), and $t = 44$ s (right). In both cases, the original contour is plotted in black, the same contour rotated by $-2\pi/3$ rad (i.e. rotation in the clockwise direction) in red, and the contour rotated $2\pi/3$ rad (anticlockwise) in blue. At $t = 44$ s, one arm has been entrained through the avalanche an additional time, leading to a crevice in this arm near the central core.

parallel to the adjacent wall of the triangle, culminating in a flattened top. In reality, the full triskelion structure cannot be seen, because one arm necessarily lies above the free surface, but it is interesting to observe the three-fold symmetry using this approach. At $t = 36$ s, the symmetry is almost perfect, because each arm has passed through the avalanche an equal number of times. At $t = 44$ s, one of the arms has passed through the avalanche an extra time, so the symmetry is not as good. The arm that has passed through the avalanche an extra time has a large rich crevice that penetrates closer to the central core, elongating the small particle rich arm. This emphasizes the fact that the pattern is continuing to evolve, with the best symmetries obtained when all the arms have passed through the avalanche the same number of times. The same symmetry is also evident in the experiments in figure 2, despite it being harder to generate a spatially homogeneous initial mixture.

4.5. Quantitative analysis and numerical convergence

To provide a quantitative comparison between the simulations and the experiments, this paper focusses on the small-particle concentration field. This can be approximately determined from experimental images using the following method. First, the drum is filled with a mixture of known small-particle concentration, shaken to achieve approximate uniformity and then photographed. The drum, containing this same mixture, is repeatedly shaken and photographed to reduce noise. This process is then repeated for a variety of mean small-particle concentrations across the range $\bar{\varphi}^s \in [0, 1]$. All the images are then cropped to remove the non-granular regions, and the colour profiles of the resulting raster images are processed in MATLAB to return a matrix giving the RGB (red-green-blue) intensities for each individual pixel. The ratio of the red intensity to the green intensity is determined for each pixel, and averaged over the entire domain. The red and green intensities exhibit a strong correlation with the mean small-particle concentration since they correspond to the colours of the small and large particles, respectively. This process returns a mean red to green pixel intensity ratio corresponding to each measured mean (over the granular domain) small-particle concentration $\bar{\varphi}^s$, and the results for a given concentration can be reliably reproduced experimentally. The ratio can then be plotted against $\varphi^s \in [0, 1]$ and a best fit

curve drawn to give a complete set of unique expected intensity ratios for every possible concentration. In fact, there is an approximately linear relationship between the intensity ratio and the particle concentration, and consequently the mapping can be further improved.

Once the relationship between the intensity ratio and the concentration is assumed to be linear, the appropriate linear fit can be determined using data taken from only two concentrations. When the mean small-particle concentration $\bar{\varphi}^s = 0$ or 1, it follows that $\varphi^s = \bar{\varphi}^s$ at every point in the granular mixture. Therefore, the images with these two mean particle concentrations can be divided into 8×8 pixel cells, where the cell size is chosen to ensure a reasonable number of particles per cell, and the concentration in every cell is known *a priori*. The mean colour intensity ratio in each individual cell is then calculated, and the mean cell intensities when $\varphi^s = 0$ and 1 can be used to produce the linear fit between intensity ratio and small-particle concentration. This method has three major advantages over using a greater number of points for $\bar{\varphi}^s$ and taking the mean pixel intensity ratio over the entire drum. First, since it uses data from 8×8 pixel cells, it can be used to derive the concentration in cells of the same size from other drum images, without any additional assumption of validity. Second, since the concentration in every cell is known when $\bar{\varphi}^s = 0$ or 1, the standard deviation of the cell intensity ratio can be trivially calculated and used to plot a set of worst fit lines which facilitate accurate error estimation. Error is due to particle shadows and uneven light reflections (Hill *et al.* 1999), which may be reduced, but not eradicated, by an appropriately positioned lighting set-up. Finally, when the drums are filled with pure phases of small or large particles, attempts at attaining a relatively homogeneous mixture are not subject to inadvertent segregation and so the colour intensity data is more reliable than for intermediate particle concentrations.

Using the calculated mapping from colour intensity to concentration, images of the developing rotating drum patterns from figure 2 are divided into 8×8 pixel cells, so that the mean red to green intensity ratio can be determined for the individual cell and a small-particle concentration value assigned using the set of expected intensity ratios. To account for the undisturbed core, which appears to have $\varphi^s = 0$ but in reality has $\varphi^s = 0.5$ due to the method of attaining the initial mixture composition (see §4.1), this region is filled with black pixels for which an exception is made so that they are assigned the correct concentration value. Note that although some pixels elsewhere in the drum appear very dark due to gaps between particles adjacent to the transparent walls, over the 8×8 pixel cells there is sufficient saturation of colour to avoid confusion with the central core region. This results in a projected small-particle concentration field for the entire drum. Using this method, the mean particle concentration of the experiments using an approximately 50:50 mixture of large and small particles is calculated to be $\bar{\varphi}^s = 0.49 \pm 0.03$, matching very closely with the approximate true value of $\bar{\varphi}^s = 0.5$.

The concentration field for the 70% filled rotating drum after $t = 48$ s is shown in figure 6. The number of pixels per cell is chosen to give a detailed concentration field with strong image definition where each cell contains many particles. The subtle region of weaker small-particle concentration above the core in the crevice of the arm being entrained into the avalanche is more clearly visible in this image than in the pre-processed image, which is shown in the final panel of figure 2. As predicted by the theory, the predominantly large particle regions adjacent to the drum walls are more strongly segregated than the small particle regions adjacent to the central core, since segregation is strongest at the free-surface, towards which the large particles are segregated. This was not evident in the pre-processed images, but has been verified by examining the field $(\varphi^s - \bar{\varphi}^s)^2$, which confirms that the predominantly large particle regions deviate further from the mean particle concentration than the predominantly small regions.

To test the strength of the segregation and compare it directly to the simulation data, the

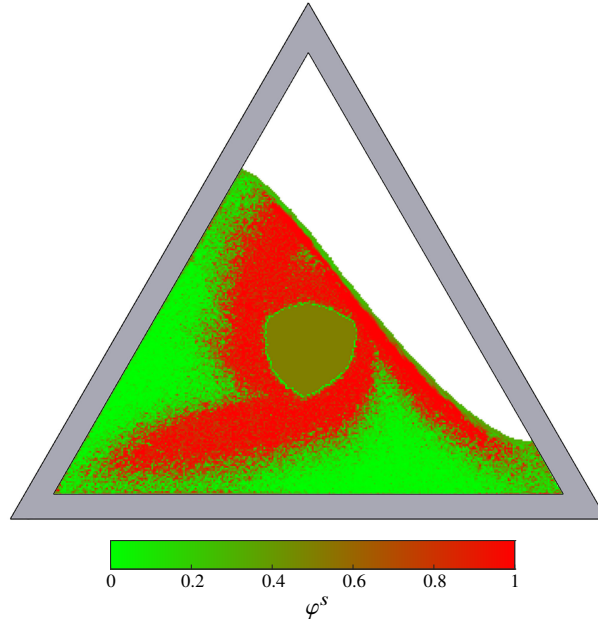


FIGURE 6: Approximated small-particle concentration field at $t = 48$ s for the experiment using a triangular drum 70% filled with an approximately 50:50 mixture of large green and small red glass beads. The small-particle concentration is obtained using the projection method described in §4.5.

segregation intensity is defined analogously to Danckwerts (1952), as the standard deviation of φ^s normalised by the mean small and large particle concentrations, $\bar{\varphi}^s(1 - \bar{\varphi}^s)$,

$$S = \sqrt{\frac{\int_{\omega} (\varphi^s - \bar{\varphi}^s)^2 dx dz}{\bar{\varphi}^s(1 - \bar{\varphi}^s) \int_{\omega} dx dz}}, \quad (4.3)$$

where ω is the part of the domain occupied by granular material. This implies that $S = 0$ for a homogeneously mixed material, and $S = 1$ when it is fully segregated. The computed and experimental segregation intensity are plotted as a function of time and at various grid resolutions in figure 7. Sidewall friction results in a free-surface avalanche that acts as a very thin boundary layer where all the segregation occurs. To correctly predict the segregation and hence the overall pattern formation, this boundary layer must be adequately resolved, which requires a very fine numerical mesh. For coarser meshes, the avalanche is under resolved and numerical diffusion therefore leads to an underestimation of the segregation intensity. Although the finest resolution, which uses 600^2 triangular cells, is not perfectly resolved, the two finest meshes yield similar results, and the time-evolution of the segregation intensities demonstrates convergence of the solution with increasing refinement. Furthermore, the simulations appear to be converging on a solution within the error bounds of that derived from experiments. This comparison confirms the earlier observation that the segregation takes place over a similar timescale in simulations and experiments, even when the avalanche is severely under resolved. This means that the numerical simulations provide a strong qualitative and quantitative match with experimental data without the need for any fitting parameters.

The simulation data shows periodic peaks and troughs in segregation intensity with a period of one third of a revolution. This can be expected given the variation in the avalanche

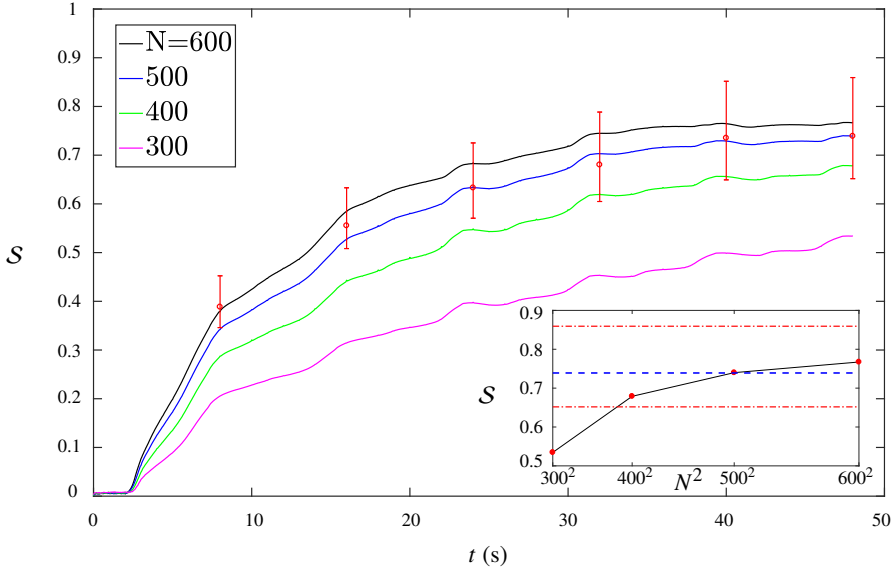


FIGURE 7: Comparison of the segregation intensity S , defined in (4.3), with time, in a 70% filled drum with a 50:50 mix of large and small particles. The experimental data is computed every third of a revolution (i.e. every 8 s) and is shown using red circles. The error bars represent the ± 1 standard deviation in the RGB intensity mapping used to determine the small particle concentration. The simulation data (coloured lines) is shown for grid resolutions $N = 300, 400, 500$ and 600 . This is equivalent to a total number N^2 mesh cells. In the inset, the segregation intensity of the simulations at $t = 48$ s is plotted against the grid resolution, with the segregation intensity calculated for the experiment represented by the dashed blue line for comparison, while the dot-dashed red lines represent the experimental error of the intensity.

dynamics with the shifting geometry (see §4.3 and figure 3), which produces higher strain-rates, longer particle trajectories through the avalanche and hence stronger segregation when the avalanche is at its longest. Both the experimental and computed segregation intensity begin to stabilize after the second revolution, with the final segregation intensity of $S = 0.77$ at $t = 48$ s at the highest resolution. After this time it will continue to plateau over many revolutions, but will never become fully periodic (Mounty 2007).

5. The importance of lateral sidewall friction

The theoretical and numerical framework used to compute the rotating drum simulation in §4 uses width-averaged, two-dimensional mass and momentum equations with Coulomb slip assumed on the transparent confining sidewalls. These sidewalls are separated by a narrow gap in experiments, in order to keep the flow fully two-dimensional, and hence allow observation of the pattern (see figure 2). It is of interest to see what effect the sidewalls have on the pattern that forms.

Figure 8(a) shows a comparison between the particle-size distribution patterns formed in the experiment in §4.1 at $t = 48$ s, and numerical simulations with and without sidewall friction. As discussed in §4.4, the simulation computed with sidewall friction matches excellently to the experimental results, without any fitting parameters. However, for the simulations without sidewall friction, almost no segregation has occurred after two drum

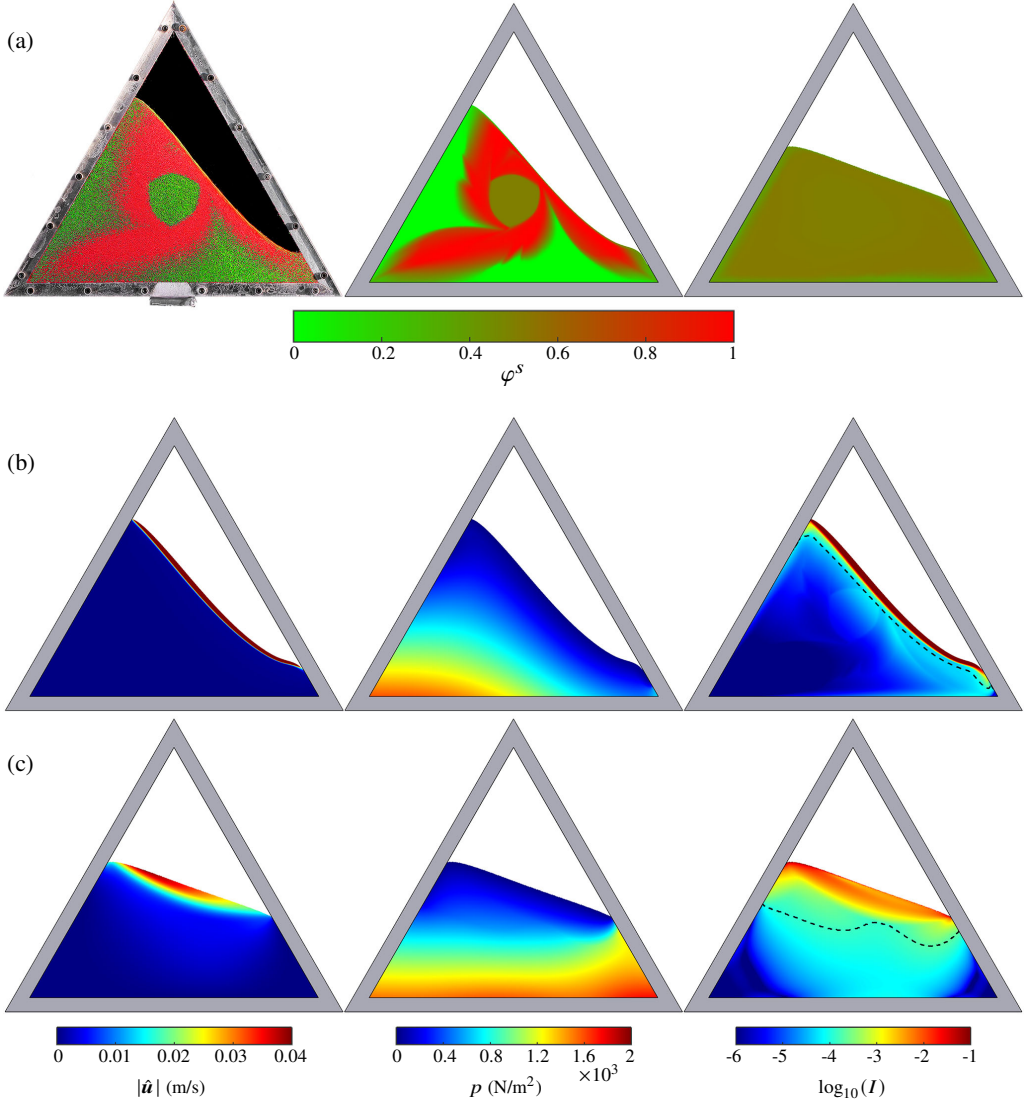


FIGURE 8: (a) Particle-size distributions in a bidisperse triangular rotating drum flow at $t = 48$ s for the experiment described in §4.1 (left), the simulation with sidewall friction (middle), and without sidewall friction (right). Movies 2, 6 and 8 show the corresponding time-dependent evolution and are available online. (b) The corresponding simulated bulk flow fields with sidewall friction and (c) without sidewall friction. The simulations without sidewall friction assume $\mu_W = 0$. The rest of the parameters are summarized in tables 1 and 2. The black dashed line indicates the position below which the high viscosity cut-off (3.9) becomes active. The particle segregation is extremely weak and the free-surface inclination angle is drastically reduced without sidewall friction.

757 revolutions. The segregation intensity is just $\mathcal{S} = 0.0663$, which indicates that there has
 758 been little deviation from the initial mixed state. A very thin region of large particles and
 759 a weaker region of small particles are discernible close to the drum walls, but in place
 760 of the triskelion pattern there is a simple triangular shape. This indicates that sidewall
 761 friction is not only a necessary consideration for accurate modelling of rotating drum

experiments performed in narrow gaps between transparent sidewalls, but is one of the dominant physical mechanisms determining the nature and extent of the segregation. At later times the segregation intensity continues to increase without sidewall friction, but even after 20 revolutions, when $S = 0.3007$, it has not reached a plateau. This indicates that the simulations without sidewall friction dramatically over estimate the segregation timescale.

In the absence of sidewall friction the free surface is straight rather than S-shaped, and the inclination angle is reduced to a value close to the static friction angle of $\zeta_s = \tan^{-1}(\mu_s) = 22^\circ$ (Barker *et al.* 2021). The bulk flow fields, with and without sidewall friction, are plotted in figures 8(b) and 8(c), respectively. Since the segregation law (2.20) is the same in both simulations, it is the differences in the bulk flow dynamics that underpins the weak segregation in the absence of sidewall friction. The peak velocity magnitude $|\hat{u}| \approx 0.14 \text{ ms}^{-1}$ without sidewall friction, which is a fivefold reduction relative to the simulation computed with sidewall friction, where $|\hat{u}| \approx 0.7 \text{ ms}^{-1}$. Overall the modulus of the relative velocity in the free-surface avalanche is about an order of magnitude smaller without sidewall friction. The avalanche is also much thicker, as predicted by the observations of Jop *et al.* (2005), and the velocity decays only gradually. The pressure field is similar, but the inertial number never approaches the high values with $I \approx 1$ observed in the presence of sidewall friction. The high viscosity cut-off is activated much deeper into the flow without sidewall friction. This reveals why the mixture segregates so weakly; the reduced strain-rate magnitude, owing to the thicker, slower flow, feeds back into the segregation scaling law (2.20) and inhibits the particle segregation. Barker *et al.* (2021) showed that this could be partially circumvented by using artificially over-sized particles, comparable to the order of magnitude to the avalanche depth. This naturally results in a more strongly segregated mixture, but nevertheless fails to predict the patterns observed in experiments with the accuracy of the computations presented in §4. The simulations in figure 8 therefore demonstrate that for rotating drum flows confined within a thin channel, it is essential that lateral sidewall friction be incorporated to capture the correct flow dynamics and the resulting particle-size segregation.

6. Varying fill fractions

The fill fraction is now varied systematically using the same homogeneous 50:50 initial mixture of large and small particles, and the same rotation rate as in §4. Figure 9 shows the experimental and computed patterns that form after two revolutions for fill levels of (a) 30%, (b) 50%, (c) 70% and (d) 80%. In comparison with the 70% filled drum discussed in §4, the homogeneous central core for the 80% filled drum is much larger due to the elevated position of the free-surface avalanche, whereas for the 30% and 50% filled drums no core forms as all the particles pass through the avalanche during each revolution.

Structurally, a similar pattern emerges for the 70% and 80% filled drums, although interestingly the homogeneous central cores appear to have opposite orientations. In fact, the corners of the central core are formed when the free-surface avalanche is longest, and therefore fastest and thickest, and the corners in the 80% filled drum are simply more subtle because the core region bulges outwards between corners. This is evident in the experiment and particularly in the numerical simulation shown in figure 9(d), which successfully capture the broad features observed experimentally. The undisturbed core is slightly larger in the simulation, suggesting the avalanche thickness is underestimated, but it accurately reproduces the shape which develops in the experiment. Unlike the 70% filled drum, the core does not approximate a Reuleaux triangle as the curvature of the sides is not approximately constant. The small-particle-rich lobes are less pronounced than for the 70% filled drum in figure 9(c), and do not exhibit the flattened tip in either simulation or experiment, instead producing a pointed tip. As shown in movies 11 and 14, the simulation at 80% fill correctly captures

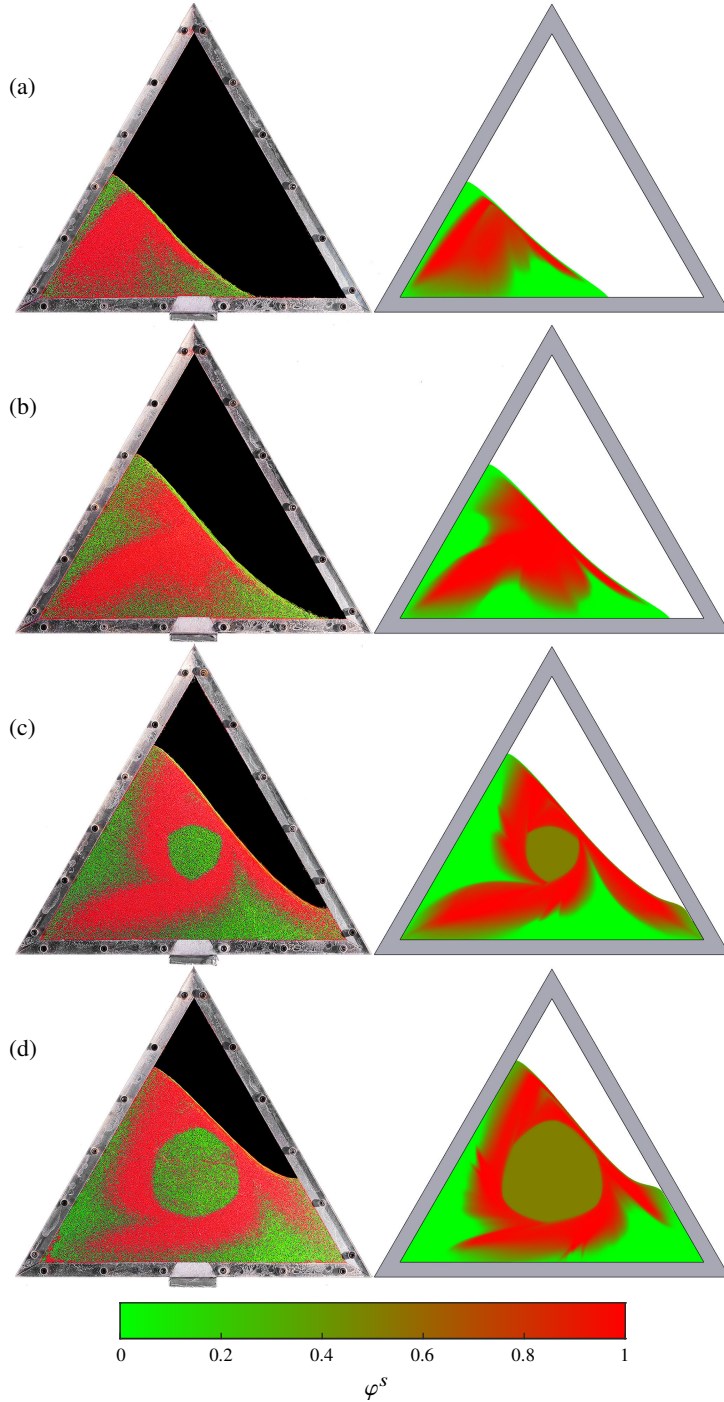


FIGURE 9: Comparison of triangular rotating drum patterns at various fill fractions for experiments (left) and computations (right). The same 50:50 mixture of large green and small red glass beads is used as in §4, and the pattern is shown after two drum revolutions at $t = 48$ s. The drums are (a) 30%, (b) 50%, (c) 70% and (d) 80% filled. Movies 2 and 6 show the existing experimental and simulated 70% filled case, while movies 9–14 show the other fill levels and are available online.

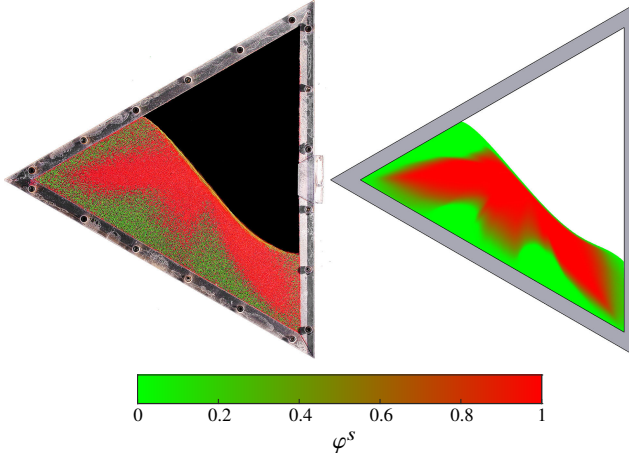


FIGURE 10: Photo of the experiment (left) and the small-particle concentration in the numerical simulation (right) of a 50% filled drum at $t = 42$ s containing a 50:50 mix of large green and small red glass beads. Two small-particle arms are distinguishable when the free surface is approximately parallel to the lower drum wall.

the time-evolution of the small particle arms, which form over the first drum revolution and become slightly shorter after subsequent re-entrainment in the second revolution. The S-shaped free-surface is reproduced very accurately by the numerical simulation, with the curvature particularly pronounced around the downslope avalanche position.

The patterns in the 30% and 50% filled drums are qualitatively very different to those discussed so far. Both cases are apparently reduced to a single small-particle lobe, which is repeatedly entrained through the free-surface avalanche and re-orientated towards the second corner of the drum frame in the clockwise direction, or by $-4\pi/3$. Furthermore, the arms have a slight arc in the anti-clockwise direction, unlike the 70% and 80% filled drums for which the arms have a clockwise arc, which is also predicted by both numerical simulations. At both 30% and 50% filled, the numerical simulation accurately captures the structure of the particle-size distribution observed in the experiment, although the S-shape of the free-surface is weaker in the former simulation. At the 30% fill level, the small-particle concentration is very strong on the outer curved edge of the arm and more diffuse towards the inside.

For the 50% filled drum, there are regions of high small-particle concentration either side of the arm near the free-surface, which would eventually coalesce into a more obvious second arm if the fill level were increased. In fact, the particle distribution structure at 50% filled is a transitional stage between the structures observed at lower and higher fill fractions, and may be said to consist of two small-particle arms. At orientations when the free-surface is approximately parallel to the lower drum wall, for example at $t = 42$ s, plotted in figure 10, there are small particle regions orientated towards both the corners of the drum occupied by granular material. These regions may be interpreted as a single arm, partially deposited downslope and partially in the upslope position, re-orientated by $-4\pi/3$ each time it passes through the avalanche. However, they should instead be identified as two genuinely distinct small particle arms re-orientated by $-2\pi/3$ after each entrainment. In figure 9(b), the second arm is undergoing entrainment through the avalanche, separated from the other by a more diffuse region.

Quantitative comparisons between the segregation intensity (4.3) in the numerical simulations and the experiments is shown in figure 11. In each case, the timescale and intensity of segregation in the simulations matches very closely with the experimental data. For both

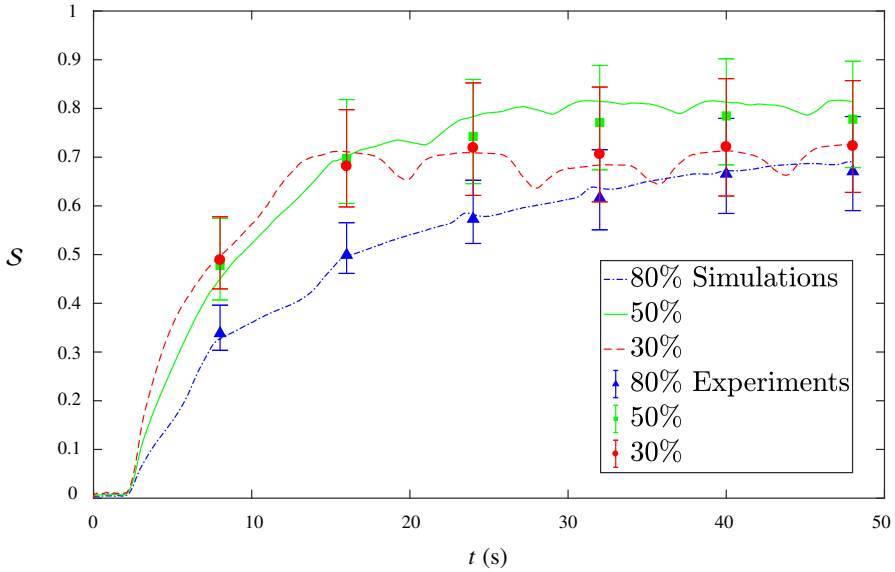


FIGURE 11: Comparison of the temporal evolution of the segregation intensity (4.3) between experiments (symbols with error bars) and numerical simulations (curves), for 80%, 50%, and 30% filled drums. A 50:50 mix of large and small particles is used in each case, and each simulation is performed with $N^2 = 600^2$ grid points.

experiments and simulations, the final segregation at $t = 48$ s is weakest at 80% fill (where $S = 0.69$, taken from the simulation data) and strongest at 50% fill ($S = 0.81$), while the 30% filled drum takes an intermediate value ($S = 0.73$). The segregation is weakest at 80% fill partly due the enlarged undisturbed central core, and may be highest at 50% fill due to the relatively small variation in the avalanche length, as can be seen in the supplementary videos. The intensity in the experiments is initially slightly stronger at 30% fill than 50% fill, before the latter case becomes significantly stronger in the second revolution of the drum. This behaviour is also predicted in the simulations, where the curves intersect near $t = 16$ s before diverging. While the 80% filled drum exhibits a relatively smooth increase with only small peaks and troughs of the segregation intensity, which very gradually plateaus, at 50% and particularly at 30% fill the intensity fluctuates more erratically. At 30% fill each peak represents a brief plateau, which actually decrease in intensity before again increasing, and the estimated intensity of the experiments broadly confirms this phenomenon since the intensity is higher at $t = 24$ s than $t = 32$ s. The peak and trough shapes of the simulation curves are heavily dependent on the fill fraction, and they also become more pronounced at a 30% fill fraction because the rotation of the drum walls dramatically alters the geometry of the enclosed granular region.

7. Varying mean particle concentrations

Attention is now turned to the dependence of the particle-size distribution and bulk flow fields on the mixture composition. Initially two further cases are examined; a 70:30 and a 30:70 mix of the of large green ($d^l = 600 - 800 \mu\text{m}$) and small red ($d^s = 300 - 400 \mu\text{m}$) particles, in addition to the original 50:50 mix. For ease of notation, these mixtures will also be referred to by the mean initial small-particle concentration, i.e. $\bar{\varphi}^s = 0.3, 0.5$ and 0.7 , respectively. In

all cases the fill level is 70%. In the experiments the same technique of shaking the drum in the horizontal orientation is used to produce an approximately homogeneous initial mixture. This time, however, the inversely graded layers of large and small particles can differ in thickness. Results from the experiments and numerical simulations are displayed in figure 12 and movies 2, 6 and 15–18.

Structurally the small particle arms are similar for each of the three mixes, and develop over the same timescale. The particle species separate out into somewhat diffuse regions over the first revolution, and then over the second revolution form a clear triskelion structure of small particle arms surrounding an undisturbed core. The different core colours in each of the numerical simulations represent the varying mean initial particle concentration. The small particle lobes are longer and thicker when the small particle content is higher, as one would expect. Furthermore, the flattened top which is nearly parallel to the adjacent drum wall can be seen very clearly in the computed solution in figure 12(c), while in figure 12(a) it is not obviously present at all. Because of the small particle arms are very thin when $\bar{\varphi}^s = 0.3$, the inner triangular region of high large particle concentration, enclosed by the core and partially entrained arm, can be seen more clearly than in the other cases. Generally the computed patterns and free-surface inclination angles are in very good agreement with the experiments, although the computed solution for $\bar{\varphi}^s = 0.7$ appears sharper than in the experiment.

The segregation scaling law (2.20) predicts that the segregation will be stronger in the highly sheared large-particle rich regions close to the avalanche surface, than in the less strongly sheared small-particle rich regions close to the avalanche base. These particle-size distributions are then preserved in the slowly rotating deposit. This is a real effect that can be seen in the experimentally derived concentration data in figure 6 in §4.5. It is also reflected in the simulations in figure 4. Varying the initial mean particle concentration provides another perspective from which to consider this phenomenon.

Figure 13(a) shows the segregation intensities at $t = 48$ s for the experiments and simulations with $\bar{\varphi}^s = 0.3, 0.5$ and 0.7 , as well as for two further extreme cases with $\bar{\varphi}^s = 0.1$ and $\bar{\varphi}^s = 0.9$. As the mean small-particle concentration increases, the mean particle size decreases, and one might reasonably expect from the scaling law (2.20) that this induces weaker overall segregation. However, the observed behaviour is significantly more complex than this. Instead, the segregation intensity initially increases with the mean small-particle concentration, up to a maximal value at $\bar{\varphi}^s = 0.5$, before it decreases for $\bar{\varphi}^s = 0.7$ and 0.9 . The segregation intensities derived from the simulation data also match closely with the experiments, confirming this general trend. The agreement between the simulations and experiments when $\bar{\varphi}^s = 0.1$ and 0.3 suggests that the value $\phi_c^s = 0.2$, which determines the point below which the segregation velocity magnitude transitions to a quadratic dependence on the grain-size ratio, is accurate. The intensity is weaker for $\bar{\varphi}^s = 0.9$ than $\bar{\varphi}^s = 0.1$, as predicted based on the respective large particle concentrations, but conversely is stronger for $\bar{\varphi}^s = 0.7$ than $\bar{\varphi}^s = 0.3$. To discern the reasons for these seemingly counter-intuitive results, it is necessary to look beyond the functional dependence of the segregation scaling law and consider the more intricate nature of segregation-mobility feedback interactions.

Hill *et al.* (1999) performed experiments for different rotating drum geometries and observed that the avalanching layer was slower and deeper for flows with larger particles. This effect is captured by Barker *et al.*'s (2021) fully coupled framework used here, since the effective friction $\mu(I)$, defined in (2.7), is a monotonically increasing in the inertial number I , which itself depends linearly on the average particle size \bar{d} , through equation (2.16). This means that (all other things being equal) larger particles are more frictional than smaller particles. In rotating drums, the mass flux in the avalanche is imposed by the rotation of the drum, so when the surface avalanche is rich in slower-moving large particles, it becomes

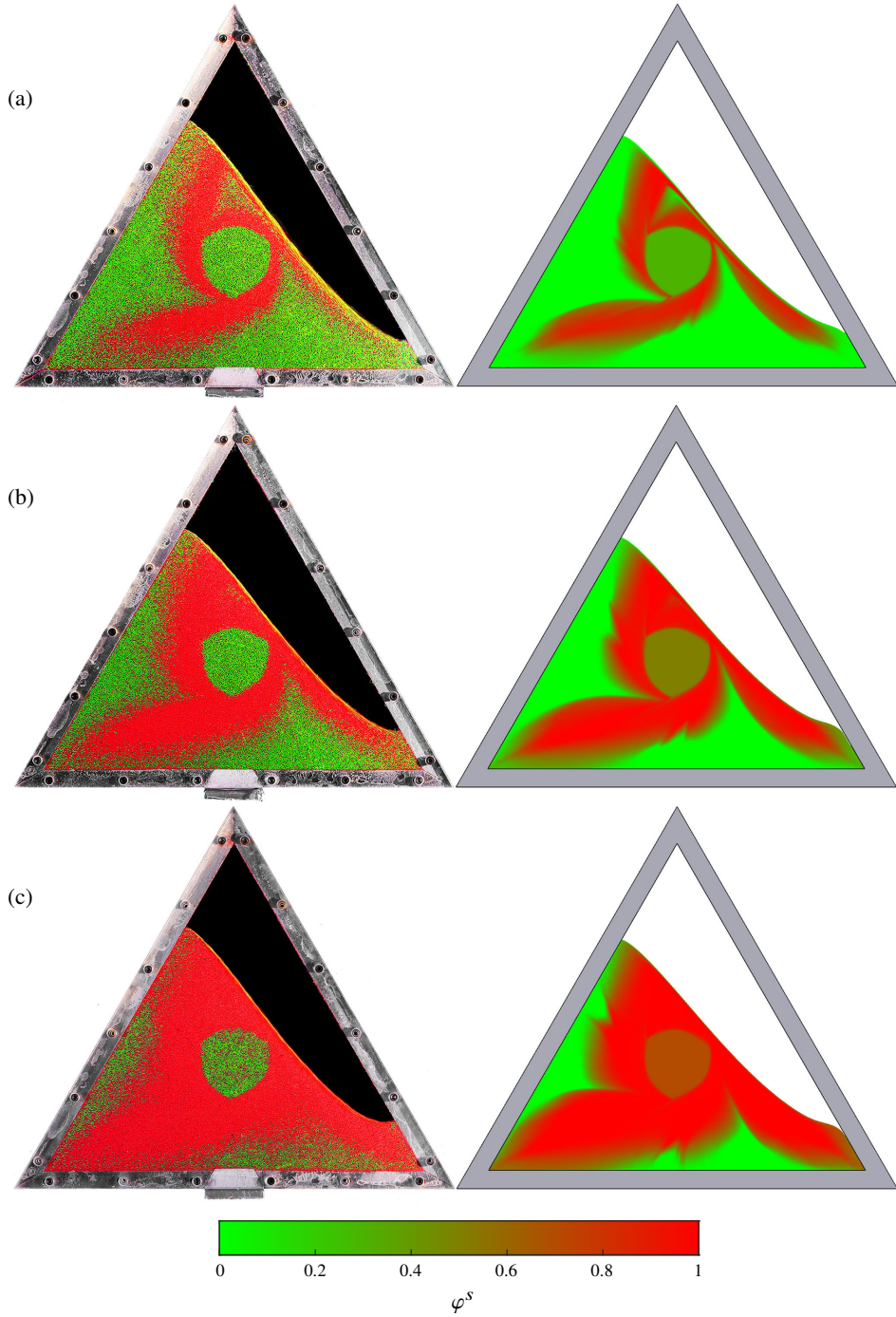


FIGURE 12: Comparison of the experimental (left) and computed (right) patterns for the case of (a) 70:30, (b) 50:50 and (c) 30:70 mixes of large green and small red glass beads in a 70% filled rotating drum. These cases are equivalently referred to as $\phi^s = 0.3, 0.5$ and 0.7 mixes. The pattern is shown after two revolutions at $t = 48$ s. Movies [2](#), [6](#) and [15–18](#) show the full time-dependent evolution of the patterns.

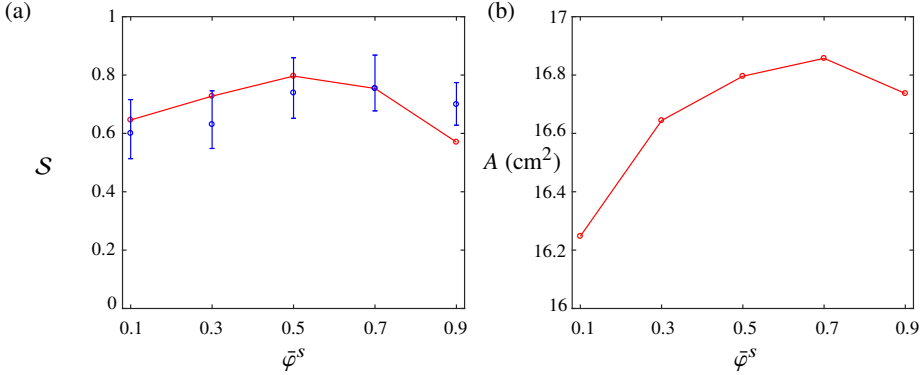


FIGURE 13: Variation of (a) the segregation intensity S , and (b) the total area of the homogeneous central core, A , as a function of the mean small-particle concentration $\bar{\varphi}^s = 0.1, 0.3, 0.5, 0.7$ and 0.9 , at $t = 48$ s. The segregation intensity is plotted for the numerical simulations (solid red circles and lines) and experiments (blue circles). The mixture with $\bar{\varphi}^s = 0.5$ segregates most strongly. The area of the homogeneous central core is plotted for the numerical simulations, and is generally smaller for flows with a higher mean concentration of large particles, due to their increased friction and deeper erosion (Hill *et al.* 1999; Barker *et al.* 2021).

deeper. As a result, the homogeneously mixed central core becomes smaller with increasing large-particle composition as shown in figure 13(b). However, the frictional feedback is even more subtle than one might at first anticipate. As the mean small-particle concentration is decreased, the friction of the mixture increases, which in turn steepens the slope inclination and hence allows the more frictional mixture to attain higher velocities. This can be seen in figure 14, which shows the relative velocity magnitude as a function of z . The differences in the composition dependent velocities are therefore not as big as one would have anticipated based on simulations on a fixed slope (Barker *et al.* 2021), but there is a very clear offset in position due to the increased slope inclination.

Although the variations in the segregation intensity in figure 13(a) are modest, the reduced value of S at low $\bar{\varphi}^s$ may therefore be attributed to the reduced shear-rate and deeper surface flows in the segregation scaling law (2.20). Conversely, at high values of $\bar{\varphi}^s$ the reduced segregation rate can be attributed to the linear dependence of (2.20) on the average particle size d . As a result, there is a point, at approximately $\bar{\varphi}^s = 0.5$, where the segregation intensity S is maximum. It is worth noting that the feedback effects of the bulk dynamics on the segregation intensity, the area of the homogeneous core and the slope inclination would not be predicted by a segregation model that used the same prescribed velocity and pressure fields in all the simulations. At 70% fill these effects are relatively small, however, there is no guarantee that they would not be more significant at other fill levels. In particular, the results of Zuriguel *et al.* (2006) in a circular drum, suggest that the system may be highly sensitive at 50% fill.

8. Segregation in a tridisperse triangular rotating drum

In the experiment shown in figure 1, a tridisperse mixture of large green ($d^l = 600 - 800 \mu\text{m}$), medium white ($d^m = 400 - 500 \mu\text{m}$) and small red ($d^s = 120 - 180 \mu\text{m}$) particles is used to generate the pattern in a 70% filled drum with a 30:40:30 mix. At the rotation rate of $\Omega = -\pi/12$ rad/s, used in the experiments and simulations in §4–7, the medium grains do not segregate into clearly discernable regions. The rotation rate is therefore reduced to $\Omega = -\pi/48$ rad/s (0.625 rpm), as medium-particle-rich regions form at this speed. The

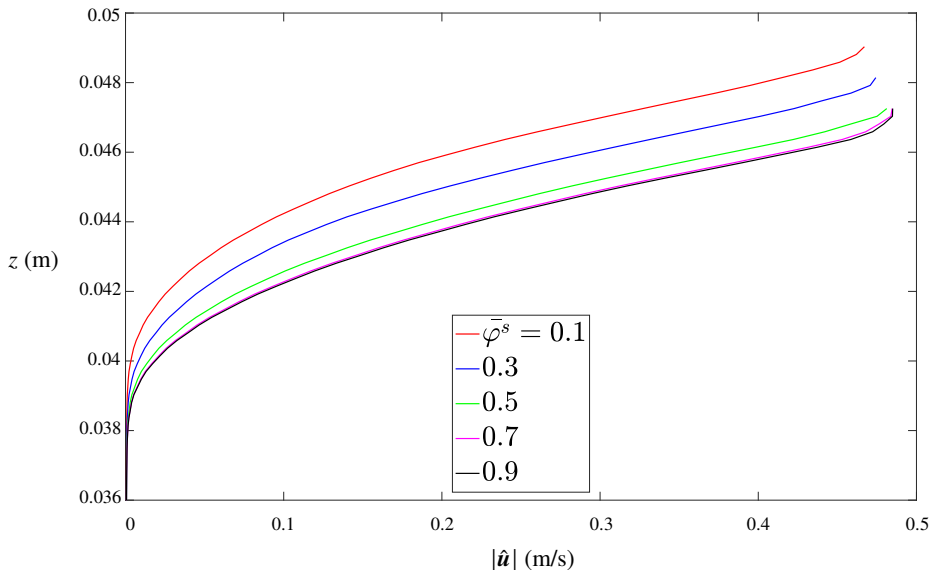


FIGURE 14: Magnitude of the relative velocity field (4.2) as a function of depth for 70% filled rotating drums with different mean particle concentrations $\bar{\varphi}^s$. The profiles are measured at the centre of the avalanche at $t = 48$ s, and cut off at the free-surface, identified by drawing the contour for $\varphi^a = 0$. The vertical offset of the plots is due to the increased slope inclination as $\bar{\varphi}^s$ is decreased.

$$d^s = 0.15 \times 10^{-3} \text{ m}, \quad d^m = 0.45 \times 10^{-3} \text{ m}, \quad d^l = 0.7 \times 10^{-3} \text{ m}.$$

TABLE 3: Grain diameters for the small, medium and large particle species used in the numerical simulations in §8.

941 reason for this is that the reduced rotation rate makes the avalanche thinner, which increases
 942 the Péclet number for segregation, $Pe_{v\lambda} = f_{v\lambda}/D_{v\lambda}$, due to the reduced pressure in the
 943 segregation scaling law (2.20). Increasing the Péclet number is equivalent to strengthening
 944 the segregation, as it compares the relative strength of the segregation to the diffusion. The
 945 full time-dependent evolution of the pattern is available in movie 1.

946 The theory in §2, is sufficiently general to model this case using the same parameters as
 947 in tables 1 and 2, and with the mean diameters specified in table 3. The numerical method
 948 in OpenFOAM is implemented for an arbitrary multi-component mixture and hence requires
 949 only the specification of an additional granular phase. Rather than describing the full set of
 950 advection-segregation-diffusion equations, which are analogous to the system of equations
 951 (3.4)-(3.7), for brevity only the segregation and diffusive fluxes will be specified. For large,
 952 medium and small granular phases and an excess air phase, denoted by the constituent letters

953 l , m , s and a , respectively, the segregation fluxes are

$$954 \quad \mathbf{F}^l = \left(-f_{ls}\varphi^l\varphi^s - f_{lm}\varphi^l\varphi^m + f_{ag}\varphi^l\varphi^a \right) \frac{\mathbf{g}}{|\mathbf{g}|}, \quad (8.1)$$

$$955 \quad \mathbf{F}^m = \left(-f_{ms}\varphi^m\varphi^s + f_{ml}\varphi^m\varphi^l + f_{ag}\varphi^m\varphi^a \right) \frac{\mathbf{g}}{|\mathbf{g}|}, \quad (8.2)$$

$$956 \quad \mathbf{F}^s = \left(f_{sm}\varphi^s\varphi^m + f_{sl}\varphi^s\varphi^l + f_{ag}\varphi^s\varphi^a \right) \frac{\mathbf{g}}{|\mathbf{g}|}, \quad (8.3)$$

$$957 \quad \mathbf{F}^a = -f_{ag}\varphi^a\varphi^g \frac{\mathbf{g}}{|\mathbf{g}|}, \quad (8.4)$$

958 and the diffusive fluxes are

$$959 \quad \mathcal{D}^l = \mathcal{D}_{ls} \left(\varphi^s \nabla \varphi^l - \varphi^l \nabla \varphi^s \right) + \mathcal{D}_{lm} \left(\varphi^m \nabla \varphi^l - \varphi^l \nabla \varphi^m \right), \quad (8.5)$$

$$960 \quad \mathcal{D}^m = \mathcal{D}_{ms} \left(\varphi^s \nabla \varphi^m - \varphi^m \nabla \varphi^s \right) + \mathcal{D}_{ml} \left(\varphi^l \nabla \varphi^m - \varphi^m \nabla \varphi^l \right), \quad (8.6)$$

$$961 \quad \mathcal{D}^s = \mathcal{D}_{sm} \left(\varphi^m \nabla \varphi^s - \varphi^s \nabla \varphi^m \right) + \mathcal{D}_{sl} \left(\varphi^l \nabla \varphi^s - \varphi^s \nabla \varphi^l \right), \quad (8.7)$$

$$962 \quad \mathcal{D}^a = \mathbf{0}, \quad (8.8)$$

963 where the overall concentration of grains is now

$$964 \quad \varphi^g = \varphi^s + \varphi^m + \varphi^l = 1 - \varphi^a. \quad (8.9)$$

965 The simulation runs for two full revolutions, and the results from the experiment and
 966 numerical simulation are presented in figure 15. Movies 1 and 19 show the full time-
 967 dependent evolution of the pattern. The simulations show that at the slower rotation rate
 968 ($\Omega = -\pi/48$ rad/s) the avalanche is indeed thinner, and hence the central core is slightly larger
 969 than in the bidisperse simulations with $\Omega = -\pi/12$ rad/s. Initially, no region of predominantly
 970 medium sized particles is clearly discernible, although small and large particle rich regions
 971 begin to form quickly. This is because the medium sized particles are being simultaneously
 972 segregated in opposite directions by the other two species (8.2). In the second revolution,
 973 regions of predominantly medium particles form, and the numerical simulations correctly
 974 predict that they are strongest adjacent to the inner side of the small particle arms, with
 975 weaker medium regions down the outer length. Overall, the simulations provide a very
 976 good qualitative match to the experimental particle-size distribution patterns, although the
 977 computed small and medium particle arms are larger and less pointed. The granular free
 978 surface is also slightly curved in the experiments, whereas it is almost flat in the simulations.
 979 The tridisperse simulations were the most computationally expensive in this paper, and
 980 required approximately 140,000 Central Processing Unit (CPU) hours to perform two drum
 981 revolutions using the highest resolution grid.

982 9. Conclusions and discussion

983 In this paper, a continuum model based on the polydisperse fully-coupled theory of
 984 Barker *et al.* (2021) is used to compute the particle-size segregation patterns that form
 985 in triangular rotating drum. The results are then compared to experiments performed in a
 986 narrow drum using bidisperse and tridisperse granular mixtures. The transparent confining
 987 sidewalls enable easy visualization of the resulting patterns, but also impose additional
 988 sidewall friction, which makes the flow thinner and faster than it would be in a wide drum
 989 (Hill *et al.* 1999; Jop *et al.* 2005). In order to quantitatively compare the experiments and

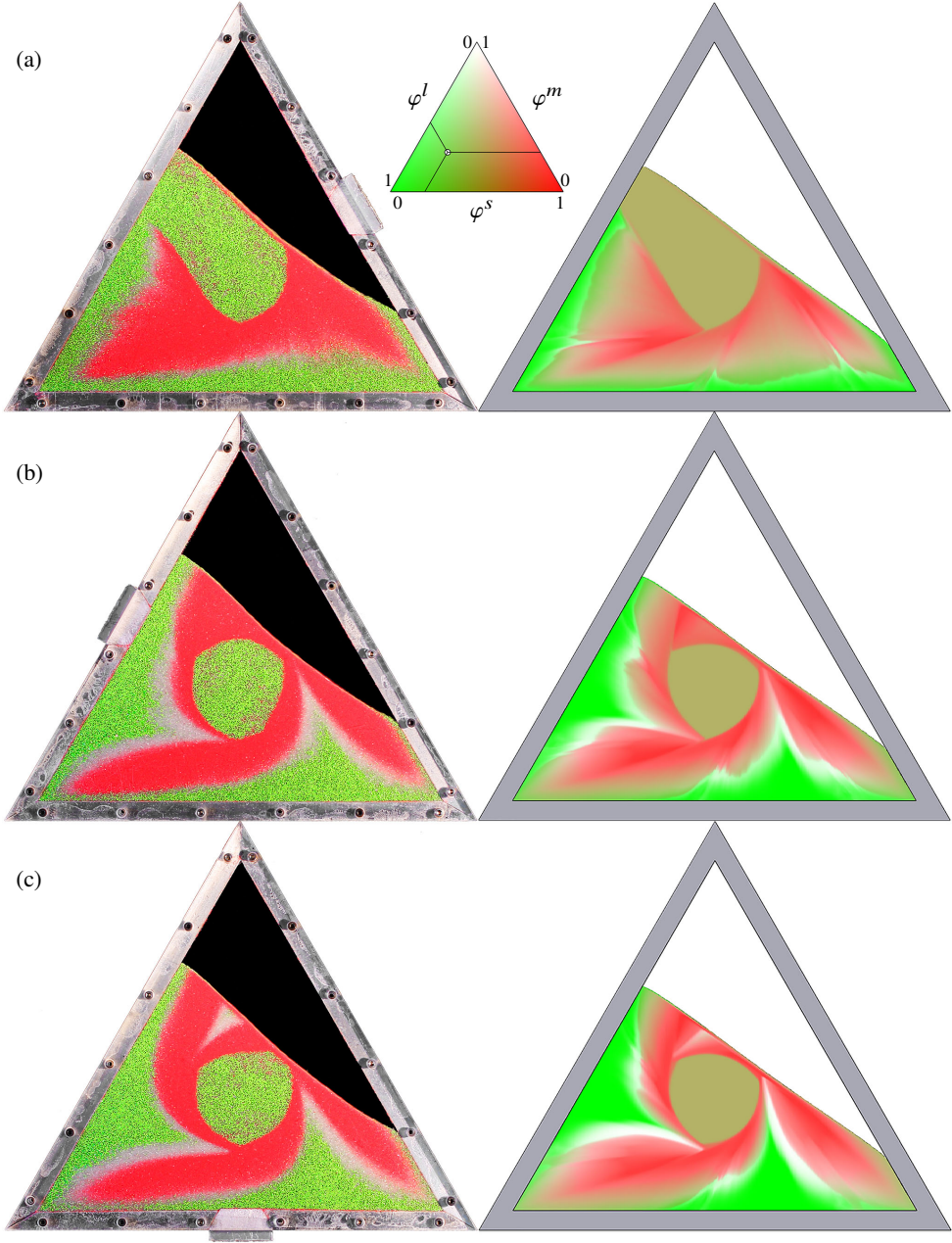


FIGURE 15: Comparison of the particle-size distribution in a 70% filled triangular rotating drum containing a tridisperse mixture of large green ($600 - 800 \mu\text{m}$), medium white ($400 - 500 \mu\text{m}$) and small red ($125 - 160 \mu\text{m}$) glass beads in 30:40:30 mix. The experiment (left) and numerical simulation (right) are shown at (a) $t = 64$ s, (b) $t = 128$ s, and (c) $t = 192$ s. Each 64 s increment represents two thirds of a revolution. The numerical particle concentrations are represented by a three-way contour scale, where the phases go from $\varphi^v = 0$ to 1. The concentration of each phase at a specific point in the triangular scale, is determined by projecting back onto the scale, parallel to the sides, as shown. The drums rotate over two full revolutions at a rotation rate of $\Omega = -\pi/48$ rad/s. Movie 1 and 19 show the full time-dependent development of the pattern in the experiment and simulation, and are available in the online supplementary material.

simulations it is therefore necessary to width average the flow, so that the sidewall friction is represented by a single term in a two-dimensional momentum balance equation (2.28).

The bidisperse width-averaged model with wall friction reproduces the observed patterns across a wide range of drum fill fractions and small particle concentrations, and quantitatively predicts how the segregation intensity evolves over time (see figures 2, 4, 7, 9, 11, 12, 13 and movies 2–7 and 9–18). In the absence of sidewall friction, the avalanche (in which segregation occurs) is predicted to be much slower and deeper, resulting in an under prediction of the segregation intensity by an order of magnitude (figure 8 and movie 8). This emphasises the critical importance of sidewall friction in modelling the flow and segregation here. The two-way coupling between flow and segregation also influences the segregation patterns. For example, an increased volume fraction of large particles results in a thicker, steeper surface avalanche (due to the particle-size dependence of the rheology), which in turn leads to weaker segregation (due to the shear-rate and pressure dependence of the segregation rate). Segregation is also weakened by the addition of a third, intermediate, grain size, and it is necessary to rotate the drum slower in order to get clearly discernable regions that are rich in medium-size grains (figures 1 and 15, and movies 1 and 19).

The results presented here demonstrate the power of the coupling method developed by Barker *et al.* (2021) and represent a strong validation of the partially regularised $\mu(I)$ -rheology and the segregation scaling law of Trewthella *et al.* (2021). The original incompressible $\mu(I)$ -rheology was derived from observations of steady-state DEM/DPM simulations and experiments on chutes and in circular rotating drums (GDR MiDi 2004; Pouliquen & Forterre 2002; Jop *et al.* 2005). Although it has been successfully applied to more complex geometries (Lacaze & Kerswell 2009; Staron, Lagr  e & Popinet 2014), it is perhaps surprising that the partially regularised theory (Barker & Gray 2017) is able to predict the bulk flow dynamics in a highly transient triangular rotating drum with such accuracy. In the bidisperse simulations, both the avalanche depth and the free-surface shape and inclination in the experiments are reproduced very closely by this rheology. Furthermore, although the segregation scaling law of Trewthella *et al.* (2021) was determined using data from refractive-index matched oscillatory shear box experiments with a single small or large particle intruder, the results presented here are only the latest successful application of this law to more complex geometries with less extreme particle concentrations (Trewthella *et al.* 2021; Barker *et al.* 2021). These results therefore suggest that the fully coupled theory used here provides a sufficient approximation of the real physics for accurate modelling of polydisperse rotating drums in the continuously avalanching or rolling regime (Rajchenbach 1990) in general. This therefore represents a major breakthrough for continuum modelling of granular flow in rotating drums. This could prove extremely useful in industrial settings where, for example, mixers fitted with segregation-inhibiting baffles (McCarthy 2009) could be tested numerically using continuum simulations before prototypes are produced.

Supplementary movies

Supplementary movies are available at <https://doi.org/10.1017/jfm.???????> and at <https://personalpages.manchester.ac.uk/staff/nico.gray/JFM2023-triangular-drum/>.

Funding

J.M.N.T. Gray was supported by a Royal Society Wolfson Research Merit Award (WM150058) and an EPSRC Established Career Fellowship (EP/M022447/1). Additional

support was provided by NERC grants NE/X00029X/1 and NE/X013936/1. All research data supporting this publication are directly available within this publication.

Declaration of Interests

The authors report no conflict of interest.

Appendix A. Shear cell with sidewall friction

Consider a semi infinite monodisperse body of grains, in a Cartesian coordinate system Oxz , enclosed between confining sidewalls and driven by a top plate moving with velocity $(V_0, 0)$ at $z = 0$. The granular material therefore occupies the region $z \leq 0$. The top plate is assumed to drive a steadily shearing velocity of the form $\mathbf{u} = (u, 0)$ in a gravity-free environment. The only non-zero component of the strain-rate tensor is $D_{xz} = (1/2)du/dz$, and hence $\|\mathbf{D}\| = (1/2)|du/dz|$. The z momentum balance implies that the pressure is equal to a constant. For incompressible models, it is necessary to specify the pressure $p = p_0$ imposed by the top plate, which then applies throughout the granular material. Since $\mathbf{u}/|\mathbf{u}| = (1, 0)$ the x momentum balance then reduces to

$$\frac{\partial \mu}{\partial z} = \frac{2}{W} \mu_W, \quad (\text{A } 1)$$

where W is the channel width and μ_W is the sidewall friction. Using the chain rule and the definition of the inertial number (2.5), this can be transformed into an ordinary differential equation (ODE) for the velocity,

$$\frac{d^2 u}{dz^2} = \frac{1}{\mu'(I)} \frac{2\mu_W}{Wd} \sqrt{\frac{p_0}{\rho_*}}, \quad (\text{A } 2)$$

where d is the grain diameter, ρ_* is the intrinsic grain density and $\mu'(I)$ is the derivative of μ with respect to I . It is possible to obtain an exact solution by invoking the $\mu(I)$ curve (2.6) of Jop *et al.* (2005). In this case μ can be differentiated to give

$$\mu'(I) = \frac{(\mu_d - \mu_s)I_0}{(I_0 + I)^2}, \quad (\text{A } 3)$$

and so after again using the definition of the inertial number (2.5), equation (A 2) becomes the second-order nonlinear ODE

$$\frac{d^2 u}{dz^2} = \beta \left(1 + \gamma \frac{du}{dz} \right)^2, \quad (\text{A } 4)$$

where β and γ are the constants

$$\beta = \frac{2\mu_W}{Wd} \left(\frac{I_0}{\mu_d - \mu_s} \right) \sqrt{\frac{p_0}{\rho_*}} \quad \text{and} \quad \gamma = \frac{d}{I_0} \sqrt{\frac{\rho_*}{p_0}}. \quad (\text{A } 5)$$

It is assumed that the material yields within a finite depth region, and therefore that the velocity is identically zero below a certain depth. Solving (A 4) subject to the boundary conditions that $u = 0$ and $du/dz = 0$ at some (as yet) unknown depth $z = -h$ implies that

$$u(z) = \frac{-\log(1 - \beta\gamma(z + h))}{\beta\gamma^2} - \frac{z + h}{\gamma}. \quad (\text{A } 6)$$

The depth h can be located exactly using the boundary condition $u = V_0$ at $z = 0$, implying

$$\log(1 - \beta\gamma h) + \beta\gamma h = -\beta\gamma^2 V_0. \quad (\text{A } 7)$$

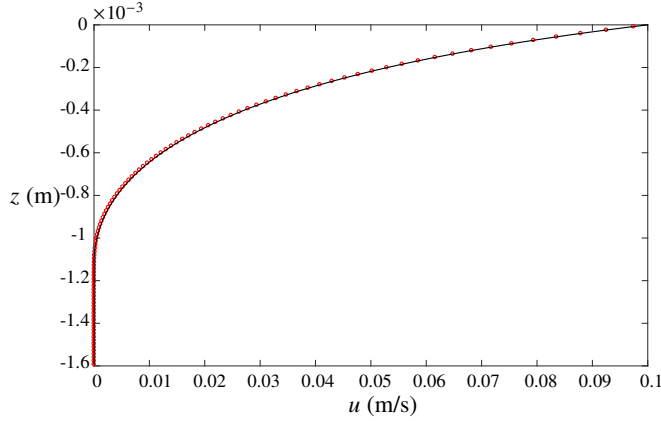


FIGURE 16: Comparison of the numerical solution computed in OpenFOAM by solving equations (3.1) and (3.2) (red open circles) to the exact solution (black curve) given by (A 6). The solution is computed using the parameters defined in table 2, and assuming that the channel width $W = 3$ mm, the wall friction coefficient $\mu_W = \tan(15.5^\circ)$, the constant pressure $p_0 = 50$ N/m² and the top plate velocity $V_0 = 0.1$ m/s. In addition, a particle diameter of $d = d^s = 0.35 \times 10^{-3}$ m was used.

This has a solution in the form of a Lambert \mathcal{W} function, and the flow depth is therefore

$$h = \frac{\mathcal{W}\left(e^{-\beta\gamma^2 V_0 - 1}\right) + 1}{\beta\gamma}. \quad (\text{A } 8)$$

A numerical solution is computed in OpenFOAM assuming a no-slip boundary condition at the base of the domain and periodic conditions on the left and right boundaries. The sidewall friction causes the velocity to rapidly decay to zero below the driving top plate, as shown in figure 16. Both the numerical and exact solutions agree very closely. In particular, the numerical simulation is able to locate the avalanche depth very accurately regardless of the extent of the domain in the z direction, i.e. if the domain extends below the position $z = -h$, the velocity u will still reduce to approximately zero at the same position. Closely related solutions also occur in vertical chutes and pipes (Barker, Zhu & Sun 2022).

REFERENCES

- ARTONI, R., LARCHER, M., JENKINS, J. T. & RICHARD, P. 2021 Self-diffusion scalings in dense granular flows. *Soft Matter* **17** (9), 2596–2602.
- BAKER, J. L., BARKER, T. & GRAY, J. M. N. T. 2016a A two-dimensional depth-averaged $\mu(I)$ -rheology for dense granular avalanches. *J. Fluid Mech.* **787**, 367–395.
- BAKER, J. L., JOHNSON, C. G. & GRAY, J. M. N. T. 2016b Segregation-induced finger formation in granular free-surface flows. *J. Fluid Mech.* **809**, 168–212.
- BANCROFT, R. S. J. & JOHNSON, C. G. 2021 Drag, diffusion and segregation in inertial granular flows. *J. Fluid Mech.* **924**, A3.
- BARKER, T. & GRAY, J. M. N. T. 2017 Partial regularisation of the incompressible $\mu(I)$ -rheology for granular flow. *J. Fluid Mech.* **828**, 5–32.
- BARKER, T., RAUTER, M., MAGUIRE, E. S. F., JOHNSON, C. G. & GRAY, J. M. N. T. 2021 Coupling rheology and segregation in granular flows. *J. Fluid Mech.* **909**, A22.
- BARKER, T., SCHAEFFER, D. G., BOHORQUEZ, P. & GRAY, J. M. N. T. 2015 Well-posed and ill-posed behaviour of the $\mu(I)$ -rheology for granular flow. *J. Fluid Mech.* **779**, 794–818.
- BARKER, T., SCHAEFFER, D. G., SHEARER, M. & GRAY, J. M. N. T. 2017 Well-posed continuum equations for granular flow with compressibility and $\mu(I)$ -rheology. *Proc. Roy. Soc. A* **473**, 20160846.

- 1094 BARKER, T., ZHU, C. & SUN, J. 2022 Exact solutions for steady granular flow in vertical chutes and pipes. *J.*
1095 *Fluid Mech.* **930**, 2021908.
- 1096 BATES, L. 1997 *User guide to segregation*. British Materials Handling Board.
- 1097 BRIDGWATER, J. 1980 Self-diffusion coefficients in deforming powders. *Powder Technol.* **25** (1), 129–131.
- 1098 BRIDGWATER, J., FOO, W. & STEPHENS, D. 1985 Particle mixing and segregation in failure zones - theory
1099 and experiment. *Powder Technol.* **41**, 147–158.
- 1100 CAI, R., XIAO, H., ZHENG, J. & ZHAO, Y. 2019 Diffusion of size bidisperse spheres in dense granular shear
1101 flow. *Phys. Rev. E* **99** (3), 032902.
- 1102 CAMPBELL, C. S. 1997 Self-diffusion in granular shear flows. *Journal of Fluid Mechanics* **348**, 85–101.
- 1103 CHIALVO, S., SUN, J. & SUNDARESAN, S. 2012 Bridging the rheology of granular flows in three regimes.
1104 *Phys. Rev. E* **85** (2), 021305.
- 1105 CLEARY, P. W. & SAWLEY, M. L. 2002 Dem modelling of industrial granular flows: 3d case studies and the
1106 effect of particle shape on hopper discharge. *Applied Math. Modelling* **26**, 89–111.
- 1107 DA CRUZ, F., EMAM, S., PROCHNOW, M., ROUX, J. N. & CHEVOIR, F. 2005 Rheophysics of dense granular
1108 materials: Discrete simulation of plane shear flows. *Phys. Rev. E* **72**, 021309.
- 1109 CUNDALL, P. A. & STRACK, O. D. L. 1979 A discrete numerical model for granular assemblies. *geotechnique*
1110 **29** (1), 47–65.
- 1111 DANCKWERTS, P. V. 1952 The definition and measurement of some characteristics of mixtures. *Appl. Sci.*
1112 *Res. A* **3** (4), 279–296.
- 1113 DENG, Z., FAN, Y., THEUERKAUF, J., JACOB, K. V., UMBANHOWAR, P. B. & LUEPTOW, R. 2020 Modeling
1114 segregation of polydisperse granular materials in hopper discharge. *Powder Tech.* **374**, 389–398.
- 1115 DENISSEN, I. F. C., WEINHART, T., TE VOORTWIS, A., LUDING, S., GRAY, J. M. N. T. & THORNTON, A. R.
1116 2019 Bulbous head formation in bidisperse shallow granular flow over an inclined plane. *J. Fluid*
1117 *Mech.* **866**, 263–297.
- 1118 DING, Y., FORSTER, R., SEVILLE, J. & PARKER, D. 2002 Granular motion in rotating drums: bed turnover
1119 time and slumping-rolling transition. *Powder Technol.* **124**, 18–27.
- 1120 DOLGUNIN, V. N. & UKOLOV, A. A. 1995 Segregation modeling of particle rapid gravity flow. *Powder*
1121 *Technol.* **83** (2), 95–103.
- 1122 EDWARDS, A., ROCHA, F., KOKELAAR, B., JOHNSON, C. & GRAY, J. 2023 Particle-size segregation in self-
1123 channelized granular flows. *J. Fluid Mech* **955**, A38.
- 1124 EDWARDS, A. N. & GRAY, J. M. N. T. 2015 Erosion-deposition waves in shallow granular free-surface flows.
1125 *J. Fluid Mech.* **762**, 35–67.
- 1126 EDWARDS, A. N., RUSSELL, A. S., JOHNSON, C. G. & GRAY, J. M. N. T. 2019 Frictional hysteresis and particle
1127 deposition in granular free-surface flows. *J. Fluid Mech.* **875**, 1058–1095.
- 1128 FAN, Y. & HILL, K. M. 2011 Theory for shear-induced segregation of dense granular mixtures. *New J. Phys.*
1129 **13** (9), 095009.
- 1130 FAN, Y., SCHLICK, C. P., UMBANHOWAR, P. B., OTTINO, J. M. & LUEPTOW, R. M. 2014 Modelling size
1131 segregation of granular materials: the roles of segregation, advection and diffusion. *J. Fluid Mech.*
1132 **741**, 252–279.
- 1133 FÉLIX, G. & THOMAS, N. 2004 Relation between dry granular flow regimes and morphology of deposits:
1134 formation of levées in pyroclastic deposits. *Earth Planet. Sci. Lett.* **221**, 197–213.
- 1135 FRY, A. M., UMBANHOWAR, P. B., OTTINO, J. M. & LUEPTOW, R. M. 2018 Effect of pressure on segregation
1136 in granular shear flows. *Phys. Rev. E* **97** (6), 062906.
- 1137 GAJJAR, P. & GRAY, J. M. N. T. 2014 Asymmetric flux models for particle-size segregation in granular
1138 avalanches. *J. Fluid Mech.* **757**, 297–329.
- 1139 GDR MiDi 2004 On dense granular flows. *Eur. Phys. J. E* **14** (4), 341–365.
- 1140 GODDARD, J. D. & LEE, J. 2017 On the stability of the $\mu(I)$ -rheology for granular flow. *J. Fluid Mech* **833**,
1141 302–331.
- 1142 GOLICK, L. A. & DANIELS, K. E. 2009 Mixing and segregation rates in sheared granular materials. *Phys.*
1143 *Rev. E* **80** (4), 042301.
- 1144 GRAY, J. & ANCEY, C. 2011 Multi-component particle-size segregation in shallow granular avalanches.
1145 *Journal of Fluid Mechanics* **678**, 535–588.
- 1146 GRAY, J. M. N. T. 2001 Granular flow in partially filled slowly rotating drums. *J. Fluid Mech.* **441**, 1–29.
- 1147 GRAY, J. M. N. T. 2018 Particle segregation in dense granular flows. *Annu. Rev. Fluid Mech.* **50**, 407–433.
- 1148 GRAY, J. M. N. T. & ANCEY, C. 2009 Segregation, recirculation and deposition of coarse particles near
1149 two-dimensional avalanche fronts. *J. Fluid Mech.* **629**, 387–423.

- GRAY, J. M. N. T. & CHUGUNOV, V. A. 2006 Particle-size segregation and diffusive remixing in shallow granular avalanches. *J. Fluid Mech.* **569**, 365–398.
- GRAY, J. M. N. T. & EDWARDS, A. N. 2014 A depth-averaged $\mu(I)$ -rheology for shallow granular free-surface flows. *J. Fluid Mech.* **755**, 503–534.
- GRAY, J. M. N. T. & HUTTER, K. 1997 Pattern formation in granular avalanches. *Continuum Mech. Thermodyn.* **9** (6), 341–345.
- GRAY, J. M. N. T. & THORNTON, A. R. 2005 A theory for particle size segregation in shallow granular free-surface flows. *Proc. Royal Soc. A* **461**, 1447–1473.
- GREVE, R. & HUTTER, K. 1993 Motion of a granular avalanche in a convex and concave curved chute: experiments and theoretical predictions. *Philos. Trans. R. Soc. London, Ser. A* **342** (1666), 573–600.
- HENEIN, H., BRIMACOMBE, J. & WATKINSON, A. 1983 Experimental study of transverse bed motion in rotary kilns. *Metall Trans. B* **14**, 191–205.
- HEYMAN, J., DELANNAY, R., TABUTEAU, H. & VALANCE, A. 2017 Compressibility regularizes the $\mu(I)$ -rheology for dense granular flows. *J. Fluid Mech.* **830**, 553–568.
- HILL, K. M., KHA KHAR, D. V., GILCHRIST, J. F., MCCARTHY, J. J. & OTTINO, J. M. 1999 Segregation-driven organization in chaotic granular flows. *Proceedings of the National Academy of Sciences* **96** (21), 11701–11706.
- HOLYOAKE, A. J. & MCELWAIN, J. N. 2012 High-speed granular chute flows. *J. Fluid Mech.* **710**, 35–71.
- ISSA, R. I. 1986 Solution of the implicitly discretised fluid flow equations by operator-splitting. *Journal of Computational Physics* **62** (1), 40–65.
- IVERSON, R. M. 2003 The debris-flow rheology myth. In *Debris-flow hazards mitigation: mechanics, prediction, and assessment*, pp. 303–314. IOS Press.
- IVERSON, R. M. & VALLANCE, J. W. 2001 New views of granular mass flows. *Geology* **29** (2), 115–118.
- JOHNSON, C. G., KOKELAAR, B. P., IVERSON, R. M., LOGAN, M., LAHUSEN, R. & GRAY, J. M. N. T. 2012 Grain-size segregation and levee formation in geophysical mass flows. *J. Geophys. Res. Earth Surf.* **117** (F01032).
- JOP, P., FORTERRE, Y. & POULIQUEN, O. 2005 Crucial role of sidewalls in granular surface flows: consequences for the rheology. *J. Fluid Mech.* **541**, 167–192.
- JOP, P., FORTERRE, Y. & POULIQUEN, O. 2006 A constitutive relation for dense granular flows. *Nature* **44**, 727–730.
- KAMRIN, K. 2019 Non-locality in granular flow: Phenomenology and modeling approaches. *Front. Phys.* **7**, 116.
- KAMRIN, K. & KOVAL, G. 2012 Nonlocal constitutive relation for steady granular flow. *Phys. Rev. Lett.* **108** (17), 178301.
- KAMRIN, K. & KOVAL, G. 2014 Effect of particle surface friction on nonlocal constitutive behavior of flowing granular media. *Comp. Particle Mech.* **1** (2), 169–176.
- KATSURAGI, H., ABATE, A. & DURIAN, D. 2010 Jamming and growth of dynamical heterogeneities versus depth for granular heap flow. *Soft Matter* **6** (13), 3023–3029.
- KETTERHAGEN, W. R., ENDE, M. T. A. & HANCOCK, B. C. 2009 Process modeling in the pharmaceutical industry using the discrete element method. *J. Pharmaceutical Sci.* **98**, 442–470.
- KHA KHAR, D. V., MCCARTHY, J. J., GILCHRIST, J. F. & OTTINO, J. M. 1999 Chaotic mixing of granular materials in two-dimensional tumbling mixers. *Chaos* **9** (1), 195–205.
- KHA KHAR, D. V., MCCARTHY, J. J. & OTTINO, J. M. 1997 Radial segregation of granular mixtures in rotating cylinders. *Phys. Fluids* **9** (12), 3600–3614.
- KOKELAAR, B. P., GRAHAM, R. L., GRAY, J. M. N. T. & VALLANCE, J. W. 2014 Fine-grained linings of leveed channels facilitate runoff of granular flows. *Earth Planet. Sci. Lett.* **385**, 172–180.
- LACAZE, L. & KERSWELL, R. R. 2009 Axisymmetric granular collapse: a transient 3d flow test of viscoplasticity. *Phys. Rev. Lett.* **102** (10), 108305.
- LAGRÉE, P.-Y., STARON, L. & POPINET, S. 2011 The granular column collapse as a continuum: validity of a two-dimensional Navier–Stokes model with a $\mu(I)$ -rheology. *J. Fluid Mech.* **686**, 378–408.
- MAKSE, H. A., HAVLIN, S., KING, P. R. & STANLEY, H. E. 1997 Spontaneous stratification in granular mixtures. *Nature* **386**, 379–382.
- MANGENEY, A., BOUCHUT, F., THOMAS, N., VILOTTE, J. P. & BRISTEAU, M. O. 2007 Numerical modeling of self-channeling granular flows and of their levee-channel deposits. *J. Geophys. Res.* **112**, F02017.
- MARTIN, N., IONESCU, I. R., MANGENEY, A., BOUCHUT, F. & FARIN, M. 2017 Continuum viscoplastic simulation of a granular column collapse on large slopes: $\mu(I)$ rheology and lateral wall effects. *Phys. Fluids* **29**, 013301.

- 1207 MAXWELL, J. C. 1867 Iv. on the dynamical theory of gases. *Philos. Trans. R. Soc. London* **157**, 49–88.
- 1208 MCCARTHY, J. J. 2009 Turning the corner in segregation. *Powder Technol.* **192** (2), 137–142.
- 1209 MELLMANN, J. 2001 The transverse motion of solids in rotating cylinders—forms of motion and transition
1210 behavior. *Powder Technol.* **118** (3), 251–270.
- 1211 MERROW, E. W. 1984 *Linking R&D to Problems Experienced in Solids Processing*. RAND Corporation,
1212 Santa Monica, CA.
- 1213 METCALFE, G., SHINBROT, T., MCCARTHY, J. & OTTINO, J. M. 1995 Avalanche mixing of granular solids.
1214 *Nature* **374** (6517), 39–41.
- 1215 MIDDLETON, G. V. 1970 Experimental studies related to problems of flysch sedimentation. In *Flysch*
1216 *Sedimentology in North America* (ed. J. Lajoie), pp. 253–272. Business and Economics Science
1217 Ltd, Toronto.
- 1218 MOUKALLED, F., MANGANI, L. & DARWISH, M. 2016 *The finite volume method in computational fluid*
1219 *dynamics*. Springer.
- 1220 MOUNTY, D. 2007 *Particle size-segregation in convex rotating drums*. PhD Thesis, The University of
1221 Manchester (United Kingdom).
- 1222 NATARAJAN, V., HUNT, M. & TAYLOR, E. 1995 Local measurements of velocity fluctuations and diffusion
1223 coefficients for a granular material flow. *J. Fluid Mech.* **304**, 1–25.
- 1224 OTTINO, J. M. & KHAKHAR, D. V. 2000 Mixing and segregation of granular materials. *Annu. Rev. Fluid*
1225 *Mech.* **32**, 55–91.
- 1226 POULIQUEN, O., DELOUR, J. & SAVAGE, S. B. 1997 Fingering in granular flows. *Nature* **386**, 816–817.
- 1227 POULIQUEN, O. & FORTERRE, Y. 2002 Friction law for dense granular flows: application to the motion of a
1228 mass down a rough inclined plane. *J. Fluid Mech.* **453**, 133–151.
- 1229 POULIQUEN, O. & VALLANCE, J. W. 1999 Segregation induced instabilities of granular fronts. *Chaos* **9** (3),
1230 621–630.
- 1231 RAJCHENBACH, J. 1990 Flow in powders: From discrete avalanches to continuous regime. *Phys. Rev. Lett.*
1232 **65** (18), 2221–2224.
- 1233 RICHARD, P., NICODEMI, M., DELANNAY, R., RIBIERE, P. & BIDEAU, D. 2005 Slow relaxation and compaction
1234 of granular systems. *Nature materials* **4**, 121–128.
- 1235 ROCHA, F. M., JOHNSON, C. G. & GRAY, J. M. N. T. 2019 Self-channelisation and levee formation in
1236 monodisperse granular flows. *J. Fluid Mech.* **876**, 591–641.
- 1237 ROGNON, P. G., ROUX, J.-N., NAAÏM, M. & CHEVOIR, F. 2007 Dense flows of bidisperse assemblies of disks
1238 down an inclined plane. *Phys. Fluids* **19** (5), 058101.
- 1239 RUSCHE, H. 2002 *Computational fluid dynamics of dispersed two-phase flows at high phase fractions*. PhD
1240 Thesis, University of London.
- 1241 SAVAGE, S. B. & LUN, C. K. K. 1988 Particle size segregation in inclined chute flow of dry cohesionless
1242 granular solids. *J. Fluid Mech.* **189**, 311–335.
- 1243 SCHAEFFER, D. G., BARKER, T., TSUJI, D., GREMAUD, P., SHEARER, M. & GRAY, J. M. N. T. 2019 Constitutive
1244 relations for compressible granular flow in the inertial regime. *J. Fluid Mech.* **874**, 926–951.
- 1245 SCHLICK, C. P., FAN, Y., UMBANHOWAR, P. B., OTTINO, J. M. & LUEPTOW, R. M. 2015 Granular segregation
1246 in circular tumblers: theoretical model and scaling laws. *J. Fluid Mech.* **765**, 632–652.
- 1247 SCOTT, A. M. & BRIDGWATER, J. 1975 Interparticle percolation: a fundamental solids mixing mechanism.
1248 *Ind. Eng. Chem. Fundam.* **14** (1), 22–27.
- 1249 SHINBROT, T. & MUZZIO, F. J. 2000 Nonequilibrium patterns in granular mixing and segregation. *Physics*
1250 *Today* **25 March**, 25–30.
- 1251 SILBERT, L. E., ERTAŞ, D., GREST, G. S., HALSEY, T. C., LEVINE, D. & PLIMPTON, S. J. 2001 Granular flow
1252 down an inclined plane: Bagnold scaling and rheology. *Phys. Rev. E* **64** (5), 051302.
- 1253 SOCIE, B. A., UMBANHOWAR, P., LUEPTOW, R. M., JAIN, N. & OTTINO, J. M. 2005 Creeping motion in granular
1254 flow. *Phys. Rev. E* **71**, 031304.
- 1255 STARON, L., LAGRÉE, P.-Y. & POPINET, S. 2012 The granular silo as a continuum plastic flow: The hour-glass
1256 vs the clepsydra. *Phys. Fluids* **24**, 103301.
- 1257 STARON, L., LAGRÉE, P.-Y. & POPINET, S. 2014 Continuum simulation of the discharge of the granular silo.
1258 *Eur. Phys. J. E* **37** (1), 5.
- 1259 TABERLET, N., RICHARD, P., VALANCE, A., LOSERT, W., PASINI, J. M., JENKINS, J. T. & DELANNAY, R. 2003
1260 Superstable granular heap in a thin channel. *Phys. Rev. Lett.* **91** (26), 264301.
- 1261 THORNTON, A. R., GRAY, J. M. N. T. & HOGG, A. J. 2006 A three-phase mixture theory for particle size
1262 segregation in shallow granular free-surface flows. *J. Fluid Mech.* **550**, 1–25.

- 1263 THORNTON, A. R., WEINHART, T., LUDING, S. & BOKHOVE, O. 2012 Modeling of particle size segregation:
1264 calibration using the discrete particle method. *Int. J. Mod. Phys. C* **23** (08), 1240014.
- 1265 TREWHELA, T., ANCEY, C. & GRAY, J. 2021 Scalings laws for gravity driven particle size segregation in
1266 dense sheared granular flows. *J. Fluid Mech.* .
- 1267 TRIPATHI, A. & KHAKHAR, D. V. 2011 Rheology of binary granular mixtures in the dense flow regime. *Phys.*
1268 *Fluids* **23** (11), 113302.
- 1269 TRIPATHI, A. & KHAKHAR, D. V. 2013 Density difference-driven segregation in a dense granular flow. *J.*
1270 *Fluid Mech.* **717**, 643–669.
- 1271 UTTER, B. & BEHRINGER, R. P. 2004 Self-diffusion in dense granular shear flows. *Phys. Rev. E* **69**, 031308.
- 1272 VAN DER VAART, K., GAJJAR, P., EPELY-CHAUVIN, G., ANDREINI, N., GRAY, J. M. N. T. & ANCEY, C. 2015
1273 Underlying asymmetry within particle size segregation. *Phys. Rev. Lett.* **114** (23), 238001.
- 1274 VALLANCE, J. W. & SAVAGE, S. B. 2000 Particle segregation in granular flows down chutes,. In *IUTAM*
1275 *Symposium on segregation in granular materials* (ed. A. D. Rosato & D. L. Blackmore). Kluwer.
- 1276 VO, T. T., NEZAMABADI, S., MUTABARUKA, P., DELENNE, J.-Y. & RADJAI, F. 2020 Additive rheology of
1277 complex granular flows. *Nature Communications* **11**, 1476.
- 1278 WEINHART, T., HARTKAMP, R., THORNTON, A. R. & LUDING, S. 2013 Coarse-grained local and objective
1279 continuum description of three-dimensional granular flows down an inclined surface. *Phys. Fluids*
1280 **25**, 070605.
- 1281 WELLER, H. G. 2006 Bounded explicit and implicit second-order schemes for scalar transport, report
1282 tr/hgw/06. *Tech. Rep.*. OpenCFD Ltd.
- 1283 WELLER, H. G. 2008 A new approach to vof-based interface capturing methods for incompressible and
1284 compressible flow, report tr/hgw/04. *Tech. Rep.*. OpenCFD Ltd.
- 1285 WIEDERSEINER, S., ANDREINI, N., EPELY-CHAUVIN, G., MOSER, G., MONNEREAU, M., GRAY, J. M. N. T.
1286 & ANCEY, C. 2011 Experimental investigation into segregating granular flows down chutes. *Phys.*
1287 *Fluids* **23**, 013301.
- 1288 WILLIAMS, S. C. 1968 The mixing of dry powders. *Powder Technol.* **2**, 13–20.
- 1289 WOODHOUSE, M. J., THORNTON, A. R., JOHNSON, C. G., KOKELAAR, B. P. & GRAY, J. M. N. T. 2012
1290 Segregation-induced fingering instabilities in granular free-surface flows. *J. Fluid Mech.* **709**, 543–
1291 580.
- 1292 YANG, R. Y., YU, A. B., McELROY, L. & BAO, J. 2008 Numerical simulation of particle dynamics in different
1293 flow regimes in a rotating drum. *Powder Technol.* **188** (2), 170–177.
- 1294 ZHU, H., ZHOU, Z., YANG, R. & YU, A. 2008 Discrete particle simulation of particulate systems: A review
1295 of major applications and findings. *Chem. Eng. Sci.* **63**, 5728–5770.
- 1296 ZURIGUEL, I., GRAY, J. M. N. T., PEIXINHO, J. & MULLIN, T. 2006 Pattern selection by a granular wave in a
1297 rotating drum. *Phys. Rev. E* **73**, 061302.